

Quantitative magnetization transfer imaging of the brain based on balanced steady state free precession

MASTER THESIS

Monika Gloor

Supervisors:

Dr. O. Bieri, Prof. Dr. K. Scheffler, Prof. Dr. B. Krusche

University of Basel, 2007



Contents

1	Introduction	1
I	Introduction to theory	2
2	Basics of magnetic resonance imaging	2
2.1	Nuclei in a magnetic field	2
2.2	Spin statistics	3
2.3	Equation of motion for the magnetization	4
2.4	The magnetic resonance signal	4
2.5	Excitation	6
2.6	Relaxation	6
2.7	MR imaging	8
3	Pulse sequences	10
3.1	Basic terms and echo formation	10
3.1.1	Spin echo	10
3.1.2	Gradient echo	10
3.2	Steady state free precession	11
3.3	Balanced steady state free precession	11
3.3.1	Numerical simulation of the bSSFP signal	13
3.3.2	Signal equation of bSSFP	15
3.3.3	Generalized signal equation of SSFP	16
4	Magnetization transfer	17
4.1	TR dependency of the bSSFP signal	17
4.2	Origin of magnetization transfer	17
4.3	Two pool model	18
II	New methods	22
5	Two simple models	22
5.1	Special case with full saturation	22
5.2	Longitudinal and saturated fraction	23
6	Signal equation for the two pool model	25
6.1	Exchange matrix	25
6.2	BSSFP signal with MT	25
7	Materials and methods	30
7.1	Experimental basics	30
7.2	Measurements and postprocessing	30
7.3	T_1 maps	31
7.4	Parameter estimations	32

8 Results	33
8.1 Numerical simulation	33
8.2 Parameter images	34
9 Discussion of the results	40
9.1 Comparison with literature values	40
9.2 Fitting sensitivities and off-resonance effects	40
9.3 Stability analysis	41
9.4 Issues	43
10 Summary	44
11 Outlook	45
11.1 SSFP signal with MT	45
11.2 SSFP signal behavior	46

1 Introduction

Traditionally, magnetic resonance imaging (MRI) generates image contrasts representing proton densities or relaxation behaviors of a sample. Some characteristics of biological tissues, however, can not be detected with traditional MRI. Tissues consist of protons free in their movement (Brownian motion) and of ones that are restricted in their motion, i.e. associated with macromolecules. Since the transverse relaxation time T_2 of bound protons is typically less than $100\ \mu\text{s}$ (T_2 of free protons $\approx 100\ \text{ms}$), standard methods are insensitive to their concentration. In contrast, magnetization transfer (MT) imaging is sensitive to the restricted proton fraction and it was suggested to be used for the diagnosis of multiple sclerosis (MS). MS is a central nervous system disease leading to a loss of myelin and thus to a loss of protons bound to myelin. The evolution of demyelination, i.e. a lesion, in the brain can be observed by MT imaging whereas it can be invisible in standard MRI.

The magnetization transfer phenomenon is often reduced to a single value, the so-called magnetization transfer ratio (*MTR*). This value, however, reflects relaxation and exchange properties as well as imaging details and experimental conditions. Only recently it was shown that balanced steady state free precession (bSSFP) is sensitive to MT effects. In this work the possibility for quantitative MT imaging with bSSFP is investigated.

For quantification of magnetization transfer, a two pool model is used. Image parameter variations in series of 3D images of the brain of healthy volunteers lead to parameter estimates for the model, i.e. the fraction of bound protons F , the exchange rates k_f and k_r between the two proton pools associated with magnetization transfer and relaxation times. Signal equations for the two pool model based on bSSFP are derived and used to fit the experimental data. Numerical simulations validate that the approximation describes the model with sufficient accuracy. Finally, the stability of quantitative MT imaging based on bSSFP is examined, providing a basis for further examinations of pathological changes.

Part I

Introduction to theory

2 Basics of magnetic resonance imaging

2.1 Nuclei in a magnetic field

If a nucleus has the angular momentum \vec{I} , its magnetic moment amounts to

$$\vec{\mu} = \gamma \vec{I} \quad \text{and} \quad |\vec{\mu}| = \gamma \hbar \sqrt{I(I+1)}, \quad (2.1)$$

where I is the nuclear spin quantum number and γ the gyromagnetic ratio ($2.6752 \cdot 10^8 \text{ s}^{-1}\text{T}^{-1}$ for hydrogen nuclei), yielding the magnetization

$$\vec{M} = \sum_{n=1}^N \vec{\mu}_n \quad (2.2)$$

for an ensemble of N spins. In an external static magnetic field of strength B_0 the potential energy of a magnetic dipole is $E = -\vec{\mu} \cdot \vec{B}_0$ and the torque is $\vec{N} = \vec{\mu} \times \vec{B}_0$. As the magnetic field tries to align the magnetic moment parallel to \vec{B}_0 , protons behave similarly to a mechanical gyroscope and precess around the magnetic field direction with the so-called Larmor frequency

$$\omega_L = \gamma B_0. \quad (2.3)$$

The magnetic moment of a nucleus with $I = 1/2$ has two possible alignments in an external magnetic field pointing in z -direction (Fig. 1). Removing the energy degeneracy leads to the nuclear Zeeman levels, which make the effect of nuclear magnetic resonance possible (Fig. 2). The magnetic moment in z -direction is related to the spin quantum number m_s

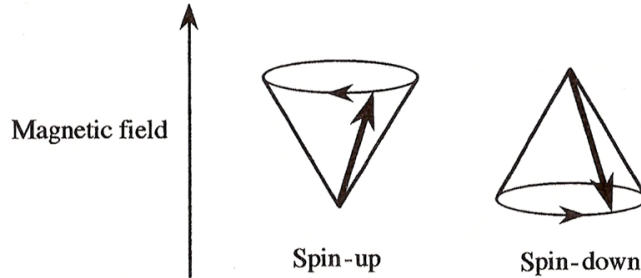


Figure 1: A spin 1/2 particle in an external magnetic field has two possible alignments [1].

by $\mu_z = \gamma \hbar m_s$. Spins parallel to the magnetic field direction have spin one half, $m_s = 1/2$, and an energy of

$$E_{\uparrow} = -\frac{1}{2} \gamma \hbar B_0. \quad (2.4)$$

Spins with $m_s = -1/2$ stand antiparallel to the field direction and have an energy of

$$E_{\downarrow} = \frac{1}{2} \gamma \hbar B_0. \quad (2.5)$$

Nuclear magnetic resonance (NMR) denotes the transition between the two eigenstates of the protons. In other words, NMR consists in flipping the magnetic moments aligned in \vec{B}_0 by irradiation of an adequate second magnetic field [1].

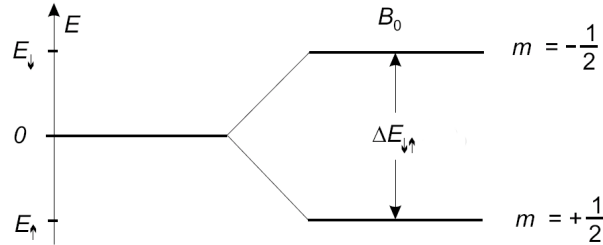


Figure 2: Nuclear Zeeman levels of a spin 1/2 particle in an external magnetic field of strength B_0 along the z -direction [23].

2.2 Spin statistics

The Boltzmann distribution describes the occupation of the energy levels by

$$\frac{n_{\uparrow}}{n_{\downarrow}} = e^{\frac{\Delta E_{\downarrow\uparrow}}{k_B T}}, \quad (2.6)$$

where n_{\uparrow} is the number of spins oriented parallel to an external field and n_{\downarrow} the number of spins oriented antiparallel to the field. Here, $\Delta E_{\downarrow\uparrow}$ is the energy difference $E_{\downarrow} - E_{\uparrow} = \gamma \hbar B_0$, k_B is the Boltzmann constant and T the temperature of the spin system. Transitions are induced by irradiating a second magnetic field of adequate frequency, according to Einstein. In thermal equilibrium there are slightly more particles in the lower energy state. In total, we therefore observe an absorption of the irradiated energy proportional to the difference in the occupation numbers, $A \propto \Delta n = n_{\uparrow} - n_{\downarrow}$ (Fig. 3).

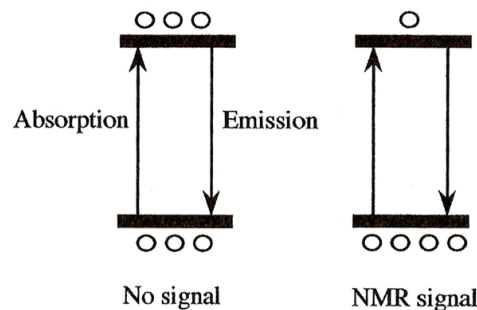


Figure 3: Formation of the magnetic resonance signal due to a difference in the occupation numbers given by the Boltzmann distribution [1].

The polarization P is given by

$$P = \frac{\Delta n}{n} = \frac{n_{\uparrow} - n_{\downarrow}}{n_{\uparrow} + n_{\downarrow}} = \frac{1 - \frac{n_{\downarrow}}{n_{\uparrow}}}{1 + \frac{n_{\downarrow}}{n_{\uparrow}}} = \frac{1 - e^{-\frac{\Delta E}{kT}}}{1 + e^{-\frac{\Delta E}{kT}}}. \quad (2.7)$$

For an MR scanner with $B_0 = 1.5$ T, we have $\Delta E \approx 10^{-27}$ J. At room temperature $kT \approx 10^{-23}$ J/K $\cdot 10^2$ K = 10^{-21} J and the absorption becomes

$$A \propto \Delta n \approx n \frac{1 - (1 - \frac{\Delta E}{kT})}{1 + (1 - \frac{\Delta E}{kT})} \approx n \frac{\Delta E}{2kT} = n \frac{\hbar \gamma B_0}{2kT}. \quad (2.8)$$

The polarization lies in the range of 10^{-6} . First, the absorption A is proportional to the number of particles n . This means that quantitative measurements concerning the proton concentration are possible. Furthermore, it is favorable to do analysis at high magnetic fields and at low temperatures. In the medical application, magnetic field and temperature are not arbitrary and therefore the very weak signal is processed by sensitive amplifiers for the imaging [1].

In the case of resonance, both energy levels are equally occupied after a very short time, and no absorption would be observed, if the Boltzman distribution was not permanently rebuilt. This happens by means of relaxation.

2.3 Equation of motion for the magnetization

The time change of the magnetic moment (Eq. (2.1)) in an external magnetic field \vec{B}_0 can be described by

$$\frac{d\vec{\mu}}{dt} = \gamma \frac{d\vec{I}}{dt} = \gamma \vec{N} = \gamma \vec{\mu} \times \vec{B}_0, \quad (2.9)$$

where \vec{N} denotes the torque on a magnetic moment in an external magnetic field (see Fig. 4). After summation, we obtain

$$\frac{d\vec{M}}{dt} = \gamma \vec{M} \times \vec{B}_0, \quad (2.10)$$

which is the equation of motion for protons that do not interact with their environment [2].

2.4 The magnetic resonance signal

As the longitudinal magnetization is negligible in comparison to the main magnetic field B_0 , irradiation with a radio frequency magnetic field, a so-called RF pulse, is necessary to rotate the longitudinal magnetization and to produce a magnetic resonance signal (MR signal). We introduce a reference frame K' , rotating around the z -axis at an angular velocity $\vec{\omega}_L$ (Fig. 5). In addition to the external magnetic field \vec{B}_0 , a nuclear momentum $\vec{\mu}$ in K' experiences the magnetic field $-\vec{\omega}/\gamma$ due to relative motion between K' and a non-rotating reference frame. Hence, the effective field is

$$\vec{B}_{eff} = \vec{B}_0 - \frac{\vec{\omega}}{\gamma} + \vec{B}_1. \quad (2.11)$$

The nuclear moment precesses with the frequency γB_{eff} in this field. The resonance condition reads $\omega = \omega_0 = \gamma B_0$, what implies $\vec{B}_{eff} = \vec{B}_1$, corresponding to the angular

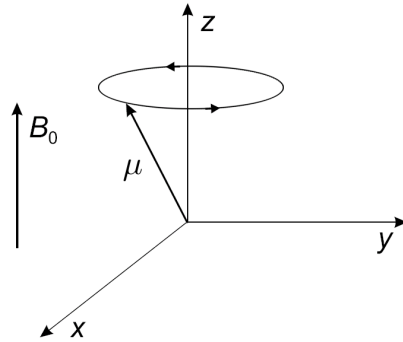


Figure 4: Precession of a magnetic moment $\vec{\mu}$ in an external magnetic field \vec{B}_0 along the z -direction [23].

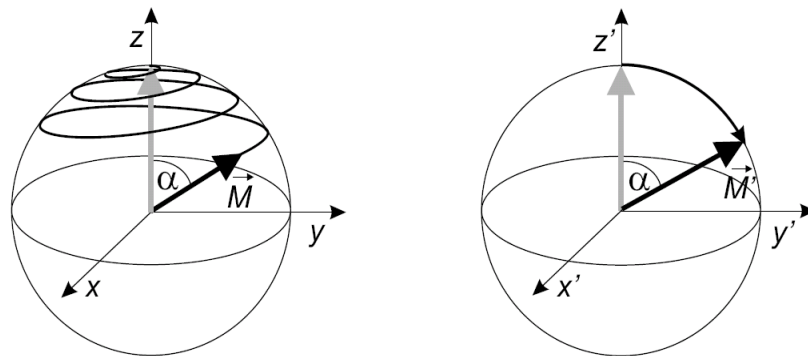


Figure 5: Movement of the magnetization vector \vec{M} in a static reference frame K (left) and a rotating reference frame K' (right) [23].

velocity ω_1 . In the rotating reference frame the magnetization is thus only exposed to \vec{B}_1 whereas \vec{B}_0 has no influence. An on-resonance pulse is an RF pulse of exactly the Larmor frequency of the precessing magnetic moment, i.e. 63.9 MHz for hydrogen nuclei in a magnetic field of 1.5 T.

2.5 Excitation

By means of an RF pulse, the magnetization is flipped away from the z -axes by an arbitrary angle, e.g. into the xy -plane (90° pulse) or into the negative z -direction (180° pulse). This process can be characterized by the flip angle (in rad)

$$\alpha = \int_0^{T_{rf}} \gamma B_1(t) dt. \quad (2.12)$$

Here, T_{rf} is the pulse duration and $B_1(t)$ the envelope of the RF pulse. If the RF pulse duration is clearly shorter than the relaxation times, $T_{rf} \ll T_1, T_2$, rotation and relaxation can be considered separately. In the following, irradiation of a magnetic field \vec{B}_1 , which is stationary in K' , is effected along the x -axis. The impact of an RF pulse of flip angle $\alpha = \omega_1 t$ can be described by the matrix

$$R_x(\alpha) = \begin{pmatrix} 1 & 0 & 0 \\ 0 & \cos \alpha & \sin \alpha \\ 0 & -\sin \alpha & \cos \alpha \end{pmatrix}. \quad (2.13)$$

Thus, the magnetization change during the short pulse duration can be written as $\vec{M}(T_{rf}) = R_x(\alpha)\vec{M}_0$. Matrix notation was first used by Jaynes in order to solve the Bloch equations [3].

2.6 Relaxation

After switching off the RF excitation, the magnetization vector \vec{M} returns to the equilibrium state \vec{M}_0 . This process is known as relaxation and the motion of the magnetization vector follows the Bloch equation

$$\frac{d\vec{M}}{dt} = \gamma \vec{M} \times \vec{B}_0 - \begin{pmatrix} \frac{M_x}{T_2} \\ \frac{M_y}{T_2} \\ \frac{M_z - M_0}{T_1} \end{pmatrix}. \quad (2.14)$$

The first term describes the classical gyroscope motion whereas the second term contains longitudinal and transverse relaxation, defined by the relaxation times T_1 and T_2 [2].

We start out of a spin system in thermal equilibrium. After an instantaneous excitation by an RF pulse, corresponding to the flip angle α , the transverse magnetization is of form $M_T(0) = M_0 \sin \alpha$. Thereafter, $M_T(t)$ decays exponentially. Transverse relaxation T_2 is also called spin-spin relaxation since it describes the loss of phase coherence between excited spins due to fluctuations in the local magnetic field. For biological tissues T_2 usually lies in the range of 30-150 ms at 1.5 T.

The longitudinal magnetization after an excitation amounts to $M_z(0) = M_0 \cos \alpha$. Through saturation (90° pulse) we obtain $M_z(0) = 0$ and through inversion (180° pulse) $M_z(0) = -M_0$. Afterwards the longitudinal magnetization heads exponentially back to its

equilibrium value M_0 . The longitudinal relaxation T_1 is also termed spin-lattice relaxation as energy is exchanged between the spin system and the surrounding thermal reservoir, the lattice. This process is controlled by transitions between Zeeman energy levels. For biological tissues T_1 lies in the range of 300-2000 ms at 1.5 T.

The three spacial components of the Bloch equation read

$$\frac{dM_x}{dt} = \omega_0 M_y - \frac{M_x}{T_2}, \quad (2.15a)$$

$$\frac{dM_y}{dt} = -\omega_0 M_x - \frac{M_y}{T_2}, \quad (2.15b)$$

$$\frac{dM_z}{dt} = \frac{M_0 - M_z}{T_1}. \quad (2.15c)$$

Substituting $M_x = m_x e^{-t/T_2}$ and $M_y = m_y e^{-t/T_2}$ leads to

$$\frac{dm_x}{dt} = \omega_0 m_y, \quad (2.16a)$$

$$\frac{dm_y}{dt} = -\omega_0 m_x. \quad (2.16b)$$

This system of coupled first order differential equations can be reduced to two decoupled second order differential equations

$$\frac{d^2 m_x}{dt^2} = -\omega_0^2 m_x, \quad (2.17a)$$

$$\frac{d^2 m_y}{dt^2} = -\omega_0^2 m_y \quad (2.17b)$$

with solution

$$M_x(t) = [M_x(0) \cos(\omega_0 t) + M_y(0) \sin(\omega_0 t)] e^{-t/T_2}, \quad (2.18a)$$

$$M_y(t) = [M_y(0) \cos(\omega_0 t) - M_x(0) \sin(\omega_0 t)] e^{-t/T_2}. \quad (2.18b)$$

The longitudinal magnetization satisfies

$$M_z(t) = M_z(0) e^{-t/T_1} + M_0 (1 - e^{-t/T_1}). \quad (2.19)$$

In a rotating frame of reference K' the first term in Eq. (2.14) vanishes, yielding

$$\frac{d}{dt} \begin{pmatrix} M_x \\ M_y \\ M_z \end{pmatrix} = - \begin{pmatrix} \frac{M_x}{T_2} \\ \frac{M_y}{T_2} \\ \frac{M_z - M_0}{T_1} \end{pmatrix}. \quad (2.20)$$

The solutions read

$$M_x(t) = M_x(0) e^{-t/T_2}, \quad (2.21a)$$

$$M_y(t) = M_y(0) e^{-t/T_2}, \quad (2.21b)$$

$$M_z(t) = M_z(0) e^{-t/T_1} + M_0 (1 - e^{-t/T_1}), \quad (2.21c)$$

and the relaxation can be expressed by the matrix

$$E(t) = \begin{pmatrix} E_2 & 0 & 0 \\ 0 & E_2 & 0 \\ 0 & 0 & E_1 \end{pmatrix}, \quad (2.22)$$

where $E_1 = e^{-t/T_1}$ and $E_2 = e^{-t/T_2}$. If the magnetization vector \vec{M}_0 is subjected only to relaxation,

$$\vec{M}(t) = E(t)\vec{M}(0) + M_0(1 - E_1)\hat{z}, \quad (2.23)$$

where \hat{z} denotes a unity vector in z -direction.

2.7 MR imaging

Generation of an MR image requires encoding of the signal with position. The principle of encoding consists in adding magnetic field gradients to B_0 , which leads to a position dependent frequency $\omega(\vec{r})$ of the magnetization. A Fourier transformation of the acquired frequency data yields the position dependent spin density $\rho(\vec{r})$.

First, consider a constant gradient \vec{G} applied during the time τ [4]. The frequency ω at position \vec{r} in the rotating frame of reference is

$$\omega(\vec{r}) = \gamma\vec{G} \cdot \vec{r}. \quad (2.24)$$

The MR signal from an element of volume dV of spins at position \vec{r} can be written as

$$dS(\vec{G}, t) = \rho(\vec{r})dV e^{i\gamma\vec{G} \cdot \vec{r}t}, \quad (2.25)$$

where $\rho(\vec{r})$ is the local spin density. The signal thus oscillates at $\gamma\vec{G} \cdot \vec{r}$ and may be integrated:

$$S(t) = \int_V \rho(\vec{r}) e^{i\gamma\vec{G} \cdot \vec{r}t} d\vec{r}, \quad (2.26)$$

where $d\vec{r}$ stands for volume integration. The concept of \vec{k} -space was introduced by Ljunggren [5]. The \vec{k} -vector is defined as

$$\vec{k} = \frac{1}{2\pi}\gamma\vec{G}t. \quad (2.27)$$

Using the \vec{k} -space formalism, the signal becomes the Fourier transform of the spin density,

$$S(\vec{k}) = \int_V \rho(\vec{r}) e^{i2\pi\vec{k} \cdot \vec{r}} d\vec{r}, \quad (2.28)$$

and the spin density is the inverse Fourier transform of the signal,

$$\rho(\vec{r}) = \int_V S(\vec{k}) e^{-i2\pi\vec{k} \cdot \vec{r}} d\vec{k}. \quad (2.29)$$

In practice, the MR signal $S(\vec{k})$ is measured at successive time intervals. The Fourier transform of this \vec{k} -space sampling yields the spin density $\rho(\vec{r})$, which is in the frequency domain and can be considered as a three-dimensional spectrum of the signal $S(\vec{k})$.

Furthermore, the volume in space can be limited by slice selection. A slice selection gradient \vec{G}_s is applied during the RF pulse irradiation. Since the Larmor frequency of the nuclear spins is proportional to the magnetic field strength, it becomes position dependent:

$$\omega_L(\vec{r}) = \gamma B_0 = \gamma \vec{G}_s \cdot \vec{r} + \omega_0, \quad (2.30)$$

where ω_0 denotes the Larmor frequency without applied gradients. The slice thickness depends on the frequency bandwidth of the RF pulse. Very short pulses are relatively broad in frequency space and consequently, many resonances at different positions are excited. Sinc-shaped pulses ($\text{sinc}(x) = \sin(x)/x$) are preferred as their Fourier transform is rectangular and therefore the slice is clearly limited. Pulses with an infinite duration are not applicable in experiments and thus sinc-pulses with one to three side lobes are used in the case of small flip angles (Fig. 6) [6]. The frequency interval $\Delta\omega$ corresponds

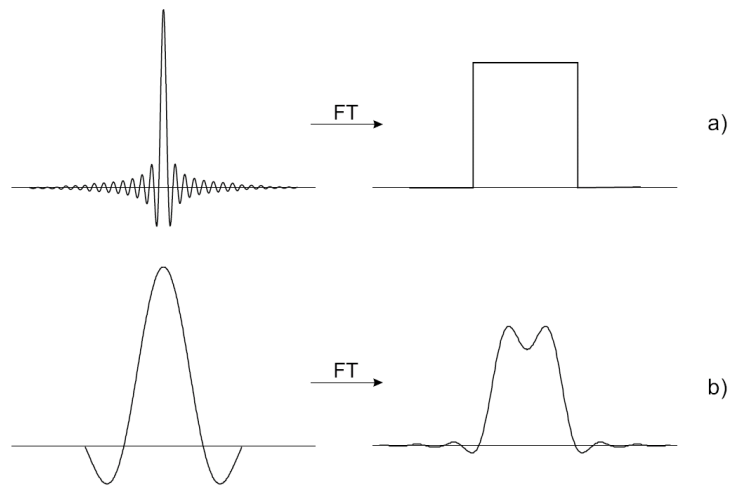


Figure 6: A sinc-pulse with infinitely many side lobes (a) and one with only one side lobe (b) as a function of time and their Fourier transforms in the frequency domain for small flip angles [23].

to the band width BW of the RF pulse and thus, the slice thickness is associated with

$$\Delta z = \frac{BW}{\gamma G_z}. \quad (2.31)$$

A frequency encoding gradient is applied along one spatial direction whereas a phase encoding gradient is applied along the other direction. Thereafter, the position of the \vec{k} -space line is well defined and read out by a readout gradient. The \vec{k} -space is sampled one line after the other.

3 Pulse sequences

3.1 Basic terms and echo formation

In practice, an image is accomplished by using a sequence of repeated RF pulses and magnetic field gradients. Depending on the sequence, RF pulses have different flip angles α , durations T_{rf} and repetition times TR . Basically, there are two types of echo formation, i.e. of signal readout.

3.1.1 Spin echo

For the spin echo, a 90° pulse is used to create the transverse magnetization. Thereafter, M_T decreases due to loss of phase coherence whereas M_z increases. At half the echo time $TE/2$ a 180° pulse is irradiated in order to refocus the proton precession by inverting the spin revolution. At TE the spin echo is read out (Fig. 7). The fast signal loss without

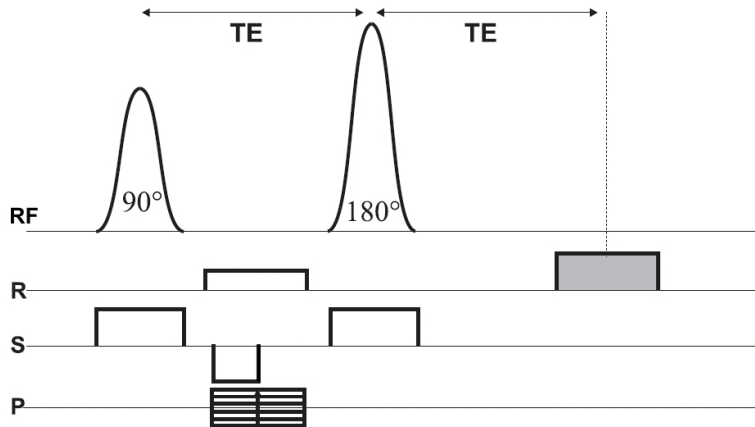


Figure 7: Spin echo with RF pulse (RF), readout gradient (R), slice selection gradient (S) and phase encoding gradient (P) [22].

refocusing, i.e. without compensating for the influence of constant inhomogeneities of the external magnetic field on the protons is described by T_2^* . The rephasing 180° pulses make the signal drop slowly with T_2 instead of T_2^* . The spin echo is comparably easy to realize and insensitive to susceptibility artifacts. However, due to long imaging times, other sequences are preferably used today.

3.1.2 Gradient echo

The gradient echo is created by application of magnetic field gradients instead of refocusing pulses. As a consequence of the omitted 180° pulses the inhomogeneities of the static magnetic field are not canceled and the signal strength is characterized by T_2^* instead of T_2 . For a homogenous magnetic field both times T_2 and T_2^* are equal. The gradient echo is characterized by a readout gradient moment which is not refocusing. After acquisition of the gradient echo, a spoiler gradient can be inserted to dephase the transverse magnetization. An example of a sequence with gradient echo is the FLASH (fast low-angle shot)

sequence (Fig. 8). This sequence uses gradient dephasing and RF spoiling, i.e. a quadratic change of the RF pulse phase.

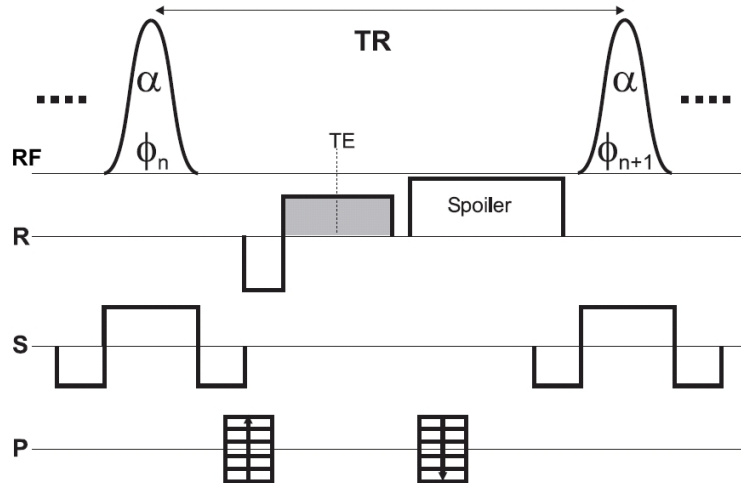


Figure 8: FLASH sequence with RF pulse (RF), readout gradient (R), slice selection gradient (S) and phase encoding gradient (P) [22].

3.2 Steady state free precession

For closely spaced successive RF pulses the MR signal never disappears entirely, what involves that the spins cannot return to the equilibrium state. In this steady state free precession (SSFP) a non-vanishing transient equilibrium state for the transverse and the longitudinal magnetization components builds up.

The signal strength depends on the repetition time TR , the type of tissue (T_1 , T_2 , ρ) and the flip angle. A steady state is reached if the flip angle α , the repetition time TR between pulses and the dephasing ϕ of spins during TR are constant. In addition, the phases of the RF pulses can vary quadratically as a function of the pulse number n as a further possibility to modify image contrast [7].

3.3 Balanced steady state free precession

Balanced steady state free precession (bSSFP) provides the highest signal of all steady state sequences. This is achieved by gradient moments adding up to zero after each sequence interval (Fig. 9). Furthermore, the bSSFP sequence is flow compensated. This means that spins with constant velocity are not subdued to any dephasing during a repetition interval. The bSSFP signal is sensitive to off-resonance effects, i.e. field inhomogeneities (Fig. 10). Hence, it is favorable to use short TR and apply a shim in order to homogenize the main magnetic field.

The signal of SSFP pulse sequences can be calculated according to the Bloch equation, Eq. (2.14). Characteristic parameters are the flip angle α , by which the magnetization is rotated due to the RF pulse, the phase angle θ of the RF pulse, which corresponds to the

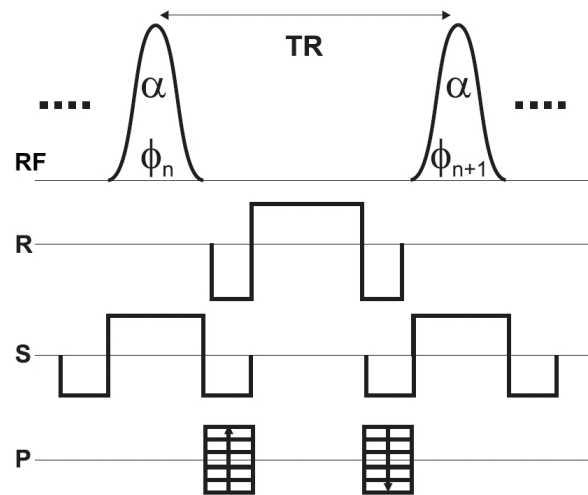


Figure 9: Balanced steady state free precession (bSSFP) sequence with RF pulse (RF), readout gradient (R), slice selection gradient (S) and phase encoding gradient (P) [22].

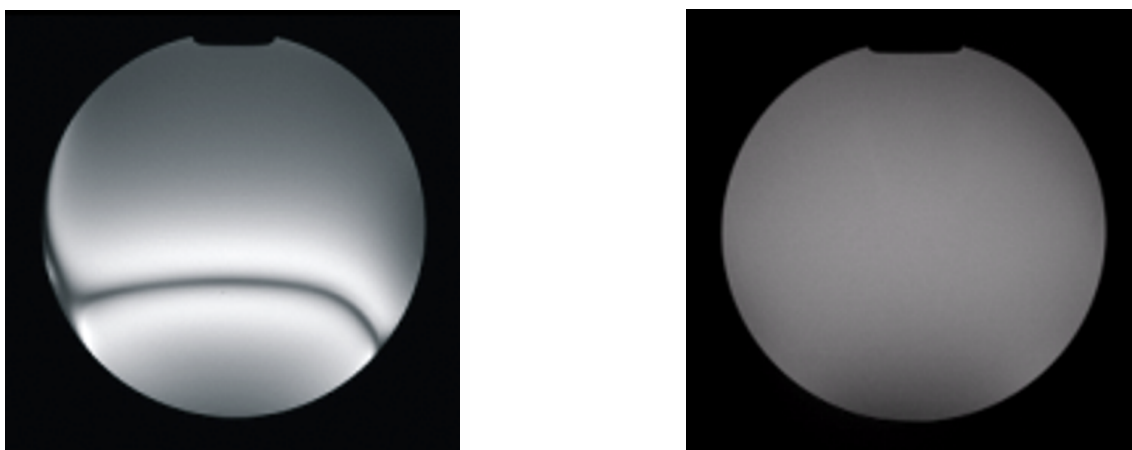


Figure 10: Left: bSSFP image with (left) and without (right) stop bands due to off-resonance effects (explanation see section 3.3.1).

direction of the irradiated field B_1 , the dephasing angle ϕ , which defines the rotation of the magnetization about the z -axis, and the relaxation, which is described by $E_1 = e^{-TR/T_1}$ and $E_2 = e^{-TR/T_2}$, respectively. Here, $\theta = 0$ means that B_1 is directed along the x -axis.

3.3.1 Numerical simulation of the bSSFP signal

The steady state MR signal can be easily simulated using rotation matrices (Eqs. (2.13) and (2.22)). First, the magnetization is rotated by a flip angle α about the x -axis, followed by relaxation during $TE = TR/2$ and rotation about the z -axis by half the phase angle $\phi/2$ due to off-resonance frequency precession. Next, the MR signal is read out. Another rotation about the z -axis by half the phase angle and relaxation during $TE = TR/2$ follow to finish TR . After several repetition cycles the magnetization vector converges into a steady state.

The absolute value of the transverse magnetization

$$|M_T| = \left| \sqrt{M_x^2 + M_y^2} \right| \quad (3.1)$$

at echo time $TE = TR/2$ can be depicted as a function of the off-resonance dephasing angle ϕ (Fig. 11). The signal curve shows 2π -periodic broad maxima, the pass bands, and narrow minima, the stop bands. The bSSFP signal depends on the flip angle as well

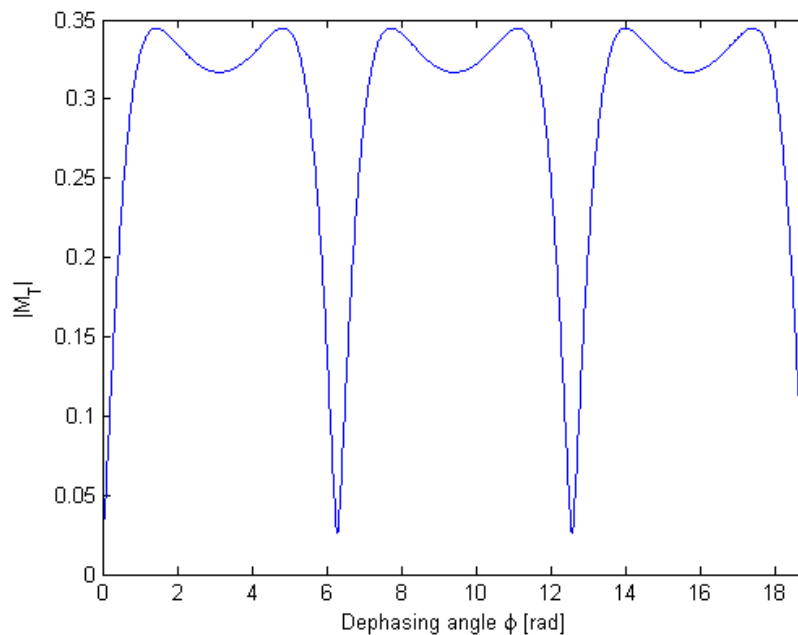


Figure 11: Transversal magnetization as a function of the off-resonance dephasing angle ϕ for $\alpha = 50^\circ$, $T_1 = 200$ ms, $T_2 = 100$ ms and $TR = 5$ ms.

(Fig. 12). For small flip angles the maximum signal is located at $\phi = 0^\circ$ and $\phi = 360^\circ$, respectively, for higher flip angles at $\phi = 180^\circ$. If α exceeds an optimal flip angle α_{opt} , the maximum gets lower. For spins with a dephasing angle of 180° the magnetization in equilibrium as a function of the flip angle α is depicted in Fig. 13.

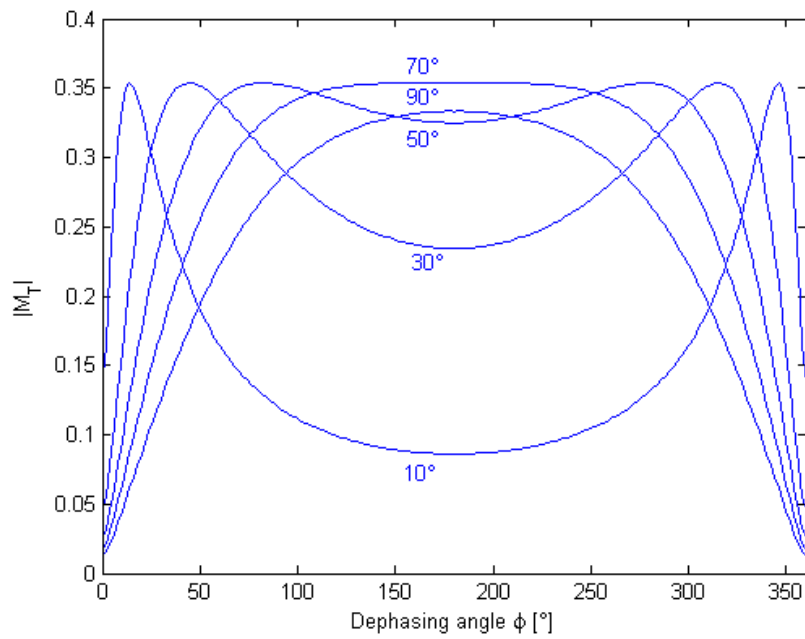


Figure 12: Transversal magnetization as a function of the dephasing angle ϕ for different flip angles, $T_1 = 200$ ms, $T_2 = 100$ ms and $TR = 5$ ms.

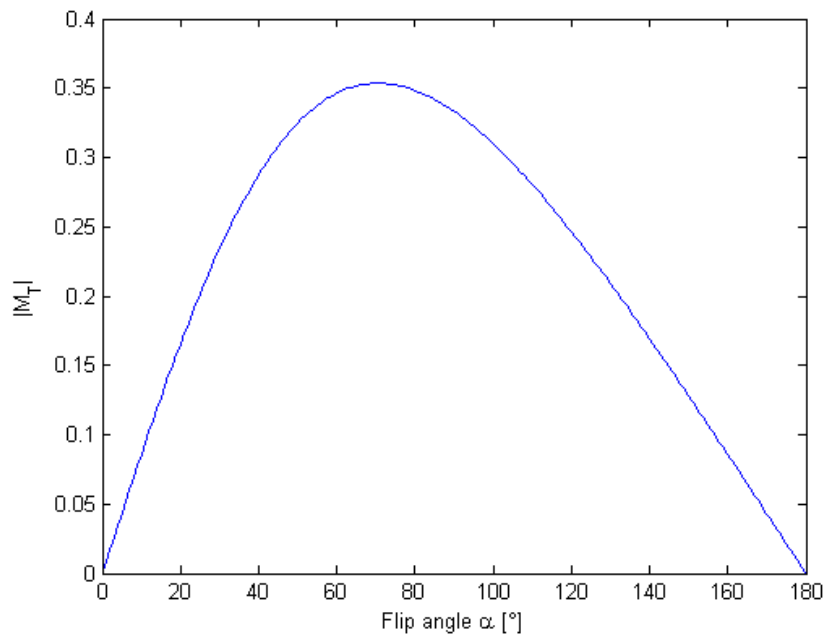


Figure 13: Transversal magnetization as a function of the flip angle α for $\phi = 180^\circ$, $T_1 = 200$ ms, $T_2 = 100$ ms and $TR = 5$ ms.

3.3.2 Signal equation of bSSFP

The evolution of the magnetization vector can be expressed by the matrices from Eqs. (2.13) and (2.22). Since partial integration was used, there is no relaxation during excitation. The magnetization directly after the n -th RF pulse is given by $\vec{M}_n^+ = R_x \vec{M}_n^-$ whereas \vec{M}_n^- expresses the magnetization directly before the n -th pulse. After the pulse and the subsequent relaxation, we get the signal directly before the $(n + 1)$ -th pulse

$$\vec{M}_{n+1}^- = E(TR)\vec{M}_n^+ + M_0(1 - E_1)\hat{z}. \quad (3.2)$$

For a steady state $\vec{M}_{n+1}^- = \vec{M}_n^-$ and thus

$$\vec{M}_n^- = \vec{M}_{n+1}^- = E(TR)R_x\vec{M}_n^- + M_0(1 - E_1)\hat{z}. \quad (3.3)$$

The steady state magnetization directly before the pulse becomes

$$\vec{M}^-(\infty) = [I - E(TR)R_x]^{-1}M_0(1 - E_1)\hat{z} \quad (3.4)$$

and the steady state magnetization directly after the pulse

$$\vec{M}^+(\infty) = R_x[I - E(TR)R_x]^{-1}M_0(1 - E_1)\hat{z}, \quad (3.5)$$

where I denotes the unity matrix. For an RF pulse along the x -axis, $M_x(\infty) = 0$ and only $M_y(\infty)$ contributes to the transverse MR signal. Solving Eq. (3.5) yields

$$M_y^+(\infty) = \frac{M_0 \sin \alpha (1 - E_1)}{1 + E_1 E_2 - (E_1 + E_2) \cos \alpha}. \quad (3.6)$$

For off-resonance precession the matrix

$$R_z(\phi) = \begin{pmatrix} \cos \phi & \sin \phi & 0 \\ -\sin \phi & \cos \phi & 0 \\ 0 & 0 & 1 \end{pmatrix} \quad (3.7)$$

is used and describes a rotation about the z -axis by the phase angle $\phi = \omega_0 t$. For the bSSFP sequence often $\phi = 180^\circ$ is used and R_z reduces to a matrix which reflects the transverse magnetization among the z -axis:

$$R_z = \begin{pmatrix} -1 & 0 & 0 \\ 0 & -1 & 0 \\ 0 & 0 & 1 \end{pmatrix}. \quad (3.8)$$

The eigenvalue equation takes the form

$$\vec{M}^+(\infty) = R_x[I - R_z E(TR)R_x]^{-1}M_0(1 - E_1)\hat{z} \quad (3.9)$$

with the solution

$$M_y^+(\infty) = \frac{M_0 \sin \alpha (1 - E_1)}{1 - E_1 E_2 - (E_1 - E_2) \cos \alpha}. \quad (3.10)$$

The bSSFP signal for on-resonance and for a centered echo ($TE = TR/2$) between alternating excitations ($\phi = 180^\circ$) is calculated according to Eq. (3.10), including the

factor $e^{-TR/(2T_2)} = \sqrt{E_2}$, which takes into account that the signal is read out at the echo time $TE = TR/2$:

$$S(\alpha, T_1, T_2, TR) = \frac{M_0 \sin \alpha (1 - E_1) \sqrt{E_2}}{1 - E_1 E_2 - (E_1 - E_2) \cos \alpha}, \quad (3.11)$$

with $E_1 = e^{-TR/T_1}$ and $E_2 = e^{-TR/T_2}$.

The signal behavior is more descriptive in the limit $TR \ll T_1, T_2$. Both E_1 and E_2 can be approximated with $1 - TR/T_1$ and $1 - TR/T_2$, respectively, and the steady state signal transforms to

$$M_y^+(\infty) = \frac{M_0 \sin \alpha}{1 + \frac{T_1}{T_2} - \left(\frac{T_1}{T_2} - 1\right) \cos \alpha}. \quad (3.12)$$

The optimal signal as a function of the flip angle for $\phi = 180^\circ$ occurs at

$$\cos \alpha_{opt} \approx \frac{\frac{T_1}{T_2} - 1}{\frac{T_1}{T_2} + 1}, \quad (3.13)$$

leading to the signal

$$M_y^+(\infty) |_{\alpha=\alpha_{opt}} = \frac{1}{2} M_0 \sqrt{\frac{T_2}{T_1}}. \quad (3.14)$$

Eq. (3.14) shows that tissues with high T_2/T_1 ratios have a high bSSFP signal [8].

3.3.3 Generalized signal equation of SSFP

In general, we have to consider the dephasing angle ϕ resulting from off-resonance effects. For a gradient echo sequence, the complex steady state transverse magnetization $M_T = M_x + iM_y$ directly after an RF pulse is

$$M_T^+(\infty) = M_0 \sin \alpha \frac{(1 - E_1)(1 - E_2 e^{-i\phi})}{C \cos \phi + D}, \quad (3.15)$$

according to [9]. Thus,

$$M_x^+(\infty) = M_0 \sin \alpha \frac{(1 - E_1)(1 - E_2 \cos \phi)}{C \cos \phi + D}, \quad (3.16)$$

and

$$M_y^+(\infty) = M_0 \sin \alpha \frac{(1 - E_1)E_2 \sin \phi}{C \cos \phi + D}, \quad (3.17)$$

where

$$C = E_2(E_1 - 1)(1 + \cos \alpha), \quad (3.18a)$$

$$D = 1 - E_1 \cos \alpha - (E_1 - \cos \alpha)E_2^2. \quad (3.18b)$$

Next, the transverse magnetization is integrated over one voxel. Only the component M_x contributes to the integral since M_y is antisymmetric due to the $\sin \phi$ term of the imaginary part.

$$\langle M_T \rangle = M_0 \frac{\sin \alpha}{2\pi} (1 - E_1) \int_{-\pi}^{\pi} \frac{1 - E_2 \cos \phi}{C \cos \phi + D} d\phi = M_0 \frac{(1 - E_1) \sin \alpha}{C} \left(\frac{C + DE_2}{\sqrt{D^2 - C^2}} - E_2 \right) \quad (3.19)$$

describes the SSFP signal.

4 Magnetization transfer

4.1 TR dependency of the bSSFP signal

According to Eq. (3.11), balanced SSFP is almost independent of TR (between $TR = 3$ ms and $TR = 20$ ms, the signal varies by less than 1%). This is confirmed in simple, i.e. aqueous, phantoms. However, it can be shown that the signal from tissues is clearly weaker than predicted by theory, i.e. from Eq. (3.11). For $TR = 3.5$ ms a contrast ratio from cerebrospinal fluid (CSF) to gray or white matter of about 6 is measured. From Eq. (3.11), however, follows a contrast ratio of about 3. On the other hand, measurements at a very long TR of 20 ms, yield a ratio of 4, being comparable to the factor 3 from theory. Thus, a considerable signal increase for long TR can be observed (Fig. 14). The origin of the signal reduction for short TR is found to be in the magnetization transfer (MT) [10].

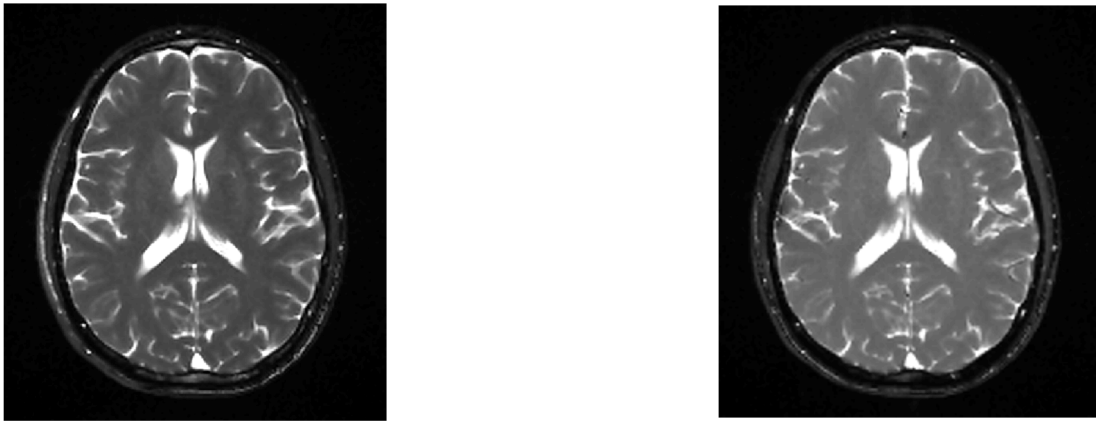


Figure 14: 2D bSSFP images with $TR = 3.5$ ms (left) and $TR = 20$ ms (right). A considerable signal decrease for short TR can be observed [10].

4.2 Origin of magnetization transfer

MT imaging was introduced by Wolff and Balaban in 1989 [11]. Magnetization transfer is based on the fact that nuclei in different chemical environments interact magnetically. In most biological tissues there are freely moving protons as well as protons bound to macromolecules or immobile protons. The bound proton (semisolid) part has a much shorter transverse relaxation time T_2 than the free proton (liquid) counterpart and it is not possible to apply spatial encoding gradients before the bound proton signal has completely decayed. The process of irradiating an RF pulse such that there is no net longitudinal magnetization is known as full saturation. Saturation of one proton pool influences the other pool. If the semisolid pool is saturated, the longitudinal magnetization of this compartment is decreased. Thus, magnetization transfer from the liquid to the semisolid pool occurs and the liquid pool becomes saturated. This results in a reduced signal from tissues exhibiting high MT. Thereby the visibility of tissues with low MT is increased (e.g. lesions and cerebral infarctions) [12]. The relaxation exchange is based on dipolar coupling or direct chemical exchange.

The signal reduction for saturation of the restricted pool is described by

$$MTR = \frac{S_0 - S_{sat}}{S_0}, \quad (4.1)$$

where S_0 is the signal without MT and S_{sat} the signal including MT. According to Eq. (4.1), a strong signal attenuation yields a high MTR . Measured MTR values depend on the applied flip angle (Fig. 15) For multiple sclerosis patients white brain matter has reduced MTR values because of a fractional demyelination and thus a loss of bound protons.

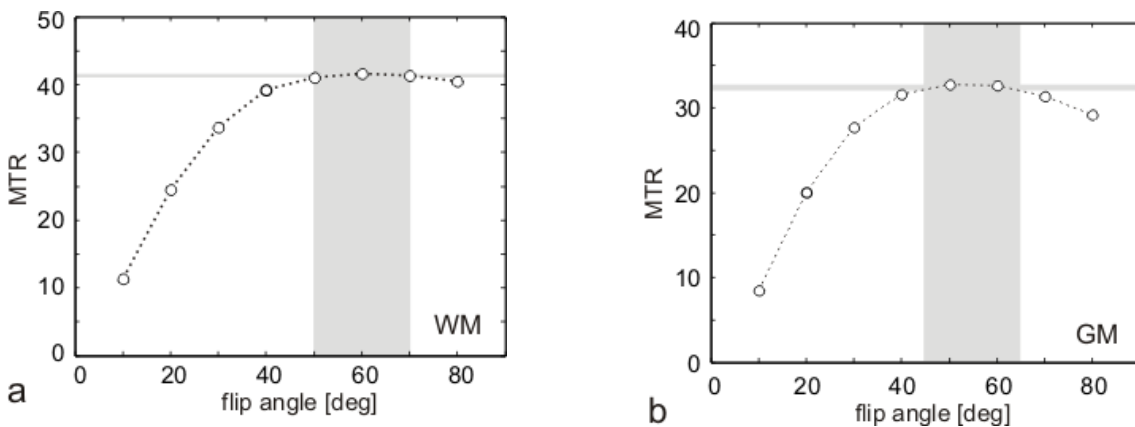


Figure 15: Measured MTR dependency on the flip angle. Maximal MTR values are achieved at $\alpha \approx 60^\circ$ and $\alpha \approx 50^\circ$ for white and gray matter, respectively. Within the gray shaded area the MTR is approximately constant.

4.3 Two pool model

Magnetization transfer simulations often base on a simple two pool model (Fig. 16), that was introduced by Henkelman et al. [13]. One pool consists of free protons (subscript f) and the other pool of protons restricted in their motion (subscript r). In each pool there is longitudinal magnetization (white), which is labeled by $M_{z,f}$ and $M_{z,r}$, respectively, and a saturated fraction (gray). The total pool sizes amount to $M_{0,f}$ and $M_{0,r}$, respectively. The rates $R_{1,f}$ and $R_{1,r}$ correspond to the recovery of the longitudinal magnetization as given by the T_1 values. Irradiating an RF pulse reduces the longitudinal magnetization by the rate $R_{RF,f}$ and $R_{RF,r}$, respectively. Furthermore, an exchange between the two compartments takes place, which is given by the rates $k_f = RM_{0,f}$ and $k_r = RM_{0,r}$.

A formal description of the two pool model bases on a coupled system of differential equations [10]. Typically, off-resonance irradiation with frequency offset Δ is used. Due to the off-resonance irradiation, the restricted pool is saturated whereas the free pool is not strongly affected (Fig. 17). The effect of a pulsed irradiation on the longitudinal magnetization of the bound protons $M_{z,r}$, according to Graham and Henkelman [15], can be described by

$$W(\Delta, t) = \pi\omega_1^2(t)G(\Delta). \quad (4.2)$$

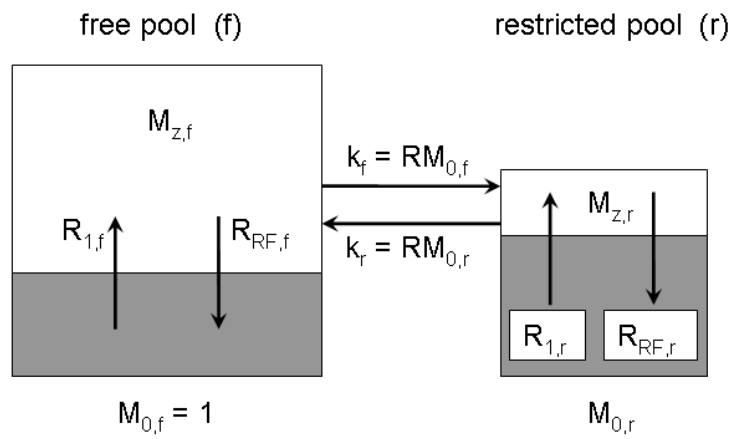


Figure 16: Two pool model including exchange between the free and the bound proton pool [13].

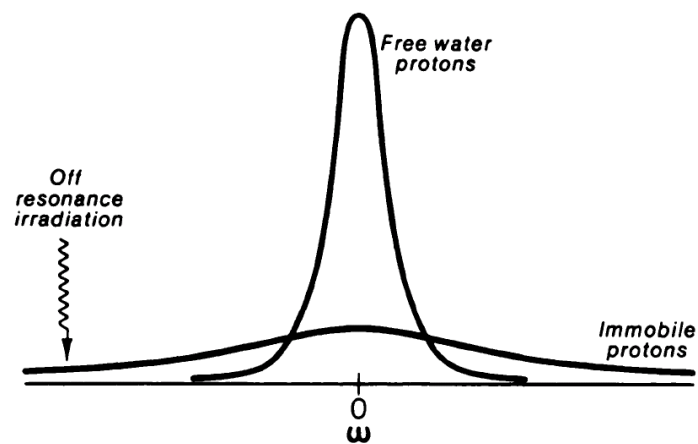


Figure 17: The bound protons have a much broader absorption lineshape than the free protons and can therefore be saturated using an off-resonance RF pulse [14].

$W(\Delta, t)$ is the time dependent saturation rate, which is proportional to the instantaneous RF pulse power $\omega_1(t) = \gamma|\vec{B}_1(t)|$ characterizing the excitation field strength, and to the absorption line shape G of the bound proton pool at a frequency offset Δ . It is found that Super-Lorentzian line shapes are appropriate for the description of tissue [16]:

$$G(2\pi\Delta) = T_{2,r} \int_0^1 \frac{1}{|3u^2 - 1|} \exp \left[-2 \left(\frac{2\pi\Delta T_{2,r}}{3u^2 - 1} \right)^2 \right] du. \quad (4.3)$$

The mean saturation rate $\langle W \rangle$ thus depends on the flip angle α , the absorption line shape G , the pulse duration T_{rf} and the pulse shape $\omega_1(t)$, and is given by

$$\langle W(\Delta) \rangle = \pi\gamma^2 \frac{1}{T_{rf}} \int_0^{T_{rf}} \omega_1^2(t) dt G(\Delta). \quad (4.4)$$

In this work, applied RF pulses are of form

$$\omega_1(t) = A \operatorname{sinc} \left[\beta \left(t - \frac{T_{rf}}{2} \right) \right] e^{-c(t-T_{rf}/2)^2}, \quad (4.5)$$

where A , β , and c are parameters that change depending on the pulse duration. If T_{rf} is stretched by the factor f , A and β are reduced by f and c by f^2 (Fig. 18).

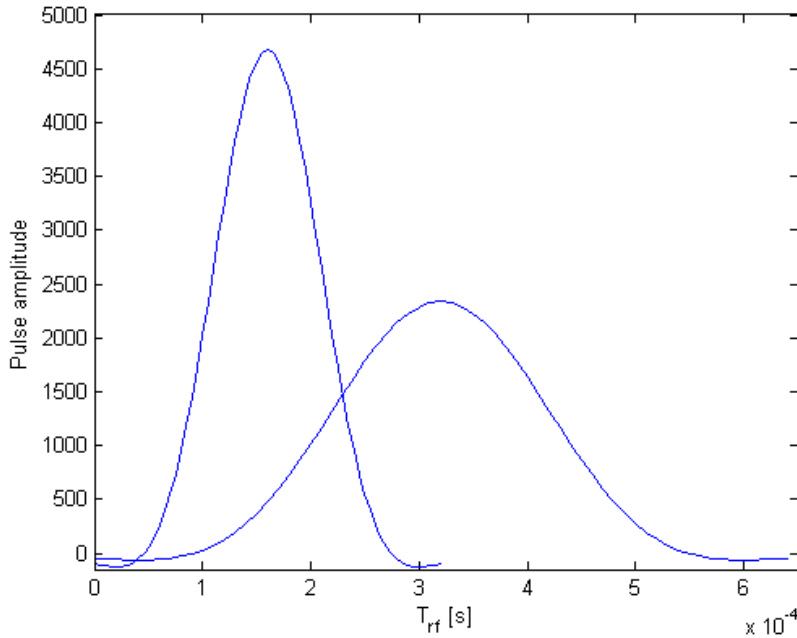


Figure 18: Shape of an RF pulse with flip angle $\alpha = 30^\circ$ and $T_{rf} = 320 \mu\text{s}$. The amplitude is halved for $T_{rf} = 640 \mu\text{s}$.

For the MT simulation with bSSFP, on-resonance irradiation is applied, i.e. $\Delta \rightarrow 0$, and G is about $1.5 \cdot 10^{-5} \text{ s}^{-1}$. The system of differential equations (see [17]) can thus be

reduced to

$$\frac{dM_{x,f}}{dt} = -\frac{M_{x,f}}{T_{2,f}}, \quad (4.6a)$$

$$\frac{dM_{y,f}}{dt} = -\frac{M_{y,f}}{T_{2,f}} + \omega_1(t)M_{z,f}, \quad (4.6b)$$

$$\frac{dM_{z,f}}{dt} = R_{1,f}(1 - M_{z,f}) - k_f M_{z,f} + k_r M_{z,r} - \omega_1(t)M_{y,f}, \quad (4.6c)$$

$$\frac{dM_{x,r}}{dt} = -\frac{M_{x,r}}{T_{2,r}}, \quad (4.6d)$$

$$\frac{dM_{y,r}}{dt} = -\frac{M_{y,r}}{T_{2,r}} + \omega_1(t)M_{z,r}, \quad (4.6e)$$

$$\frac{dM_{z,r}}{dt} = R_{1,r}(M_{0,r} - M_{z,r}) + k_f M_{z,f} - k_r M_{z,r} - W(\Delta \rightarrow 0, t)M_{z,r}. \quad (4.6f)$$

Here, $R_{1,f}$ and $R_{1,r}$ refer to the longitudinal relaxation rates, $T_{2,f}$ and $T_{2,r}$ to the transverse relaxation times and k_f and k_r to the exchange rates between the two pools. The equilibrium magnetization of the free pool $M_{0,f}$ was set equal to one. The fractional size of the restricted pool amounts to $F = M_{0,r}/M_{0,f}$ and by definition $k_r = k_f/F$. Considering that $T_{2,f}$ is very short, Eqs. (4.6d) and (4.6e) result in $M_{x,r} \approx 0$ and $M_{y,r} \approx 0$, which leaves a system of four coupled differential equations.

Part II

New methods

5 Two simple models

5.1 Special case with full saturation

In the case of two pools and flip angles $\alpha \gg 0$ full saturation of the restricted pool may occur, i.e. $M_{z,r} = 0$. Thus, the signal loss of the free pool due to magnetization transfer becomes maximal. Considering short RF pulses with $T_{rf} \ll T_1, T_2$, the rotational parts of Eqs. (4.6a), (4.6b), (4.6c) and (4.6f) take the form:

$$\frac{dM_{x,f}}{dt} = 0, \quad \text{hence } M_{x,f}(t) = M_{x,f}(0); \quad (5.1a)$$

$$\frac{dM_{y,f}}{dt} = \omega_1 M_{z,f}, \quad \text{hence } M_{y,f}(t) = M_{y,f}(0) \cos \omega_1 t + M_z(0) \sin \omega_1 t; \quad (5.1b)$$

$$\frac{dM_{z,f}}{dt} = -\omega_1 M_{y,f}, \quad \text{hence } M_{z,f}(t) = M_{z,f}(0) \cos \omega_1 t - M_y(0) \sin \omega_1 t; \quad (5.1c)$$

$$\frac{dM_{z,r}}{dt} = -W(\Delta \rightarrow 0, t) M_{z,r}, \quad \text{hence } M_{z,r}(t) = M_{z,r}(0) e^{-W(\Delta \rightarrow 0, t)t}. \quad (5.1d)$$

The equations and solutions for the relaxation are found to be:

$$\frac{dM_{x,f}}{dt} = -\frac{M_{x,f}}{T_{2,f}}, \quad \text{hence } M_{x,f}(t) = M_{x,f}(0) e^{-t/T_{2,f}}; \quad (5.2a)$$

$$\frac{dM_{y,f}}{dt} = -\frac{M_{y,f}}{T_{2,f}}, \quad \text{hence } M_{y,f}(t) = M_{y,f}(0) e^{-t/T_{2,f}}; \quad (5.2b)$$

$$\frac{dM_{z,f}}{dt} = R_{1,f}(M_{0,f} - M_{z,f}) - k_f M_{z,f}; \quad (5.3a)$$

$$\frac{dM_{z,r}}{dt} = R_{1,r}(M_{0,r} - M_{z,r}) + k_f M_{z,f}. \quad (5.3b)$$

By scaling, the z -component equation for relaxation of the free pool can be reduced to the equation already solved for the free pool alone (Eq. (2.15c)):

$$\begin{aligned} \frac{dM_{z,f}}{dt} &= R_{1,f}(M_{0,f} - M_{z,f}) - k_f M_{z,f} = R_{1,f} M_{0,f} - (R_{1,f} + k_f) M_{z,f} \\ &= (R_{1,f} + k_f) \left[\frac{R_{1,f}}{R_{1,f} + k_f} M_{0,f} - M_{z,f} \right] = \hat{R}_{1,f} (\hat{M}_{0,f} - M_{z,f}), \end{aligned}$$

with $\hat{R}_{1,f} = R_{1,f} + k_f$ and $\hat{M}_{0,f} = R_{1,f}/(R_{1,f} + k_f) M_{0,f}$. The differential equation has a solution of the same form as Eq. (2.19), if $R_{1,f}$ is replaced by $\hat{R}_{1,f}$ and $M_{0,f}$ by $\hat{M}_{0,f}$.

$$M_{z,f}(t) = M_{z,f}(0) e^{-(R_{1,f} + k_f)t} + \frac{R_{1,f}}{R_{1,f} + k_f} M_{0,f} \left(1 - e^{-(R_{1,f} + k_f)t} \right). \quad (5.4)$$

Thus, the signal equation, Eq. (3.11), can also be used in this case with the above-mentioned substitutions.

We make the approximation that the restricted pool can be considered isolated. The MTR can be calculated using the two extremal cases of no saturation and full saturation. For the one pool fraction we set $E_1 = e^{-R_1 TE}$ and $M_0 = 1$ and get the signal $S_0(\alpha)$. For the free pool in case of full saturation of the restricted pool we use $\hat{E}_1 = e^{-(R_1+k_f)TE}$ and $\hat{M}_0 = R_1/(R_1 + k_f)$ and get the signal $S_{sat}(\alpha)$. Hence the MTR follows from Eq. (4.1).

For white matter $R_1 = 1.71 \text{ s}^{-1}$, $T_{2,f} = 81 \text{ ms}$ and $k_f = 4.45 \text{ s}^{-1}$, for gray matter $R_1 = 0.97 \text{ s}^{-1}$, $T_{2,f} = 93 \text{ ms}$ and $k_f = 2.30 \text{ s}^{-1}$ were measured and simulated, respectively [18]. Furthermore, we used $TR = 3 \text{ ms}$. Calculating the MTR from this strongly simplified model yields a too high signal for $\alpha \rightarrow 0$ because the denominator $S_0(\alpha)$ becomes small (Fig. 20, left).

5.2 Longitudinal and saturated fraction

As the derived MTR values (Fig. 20, left) do not correspond to the measured values (Fig. 15), especially for small flip angles, a less simplified approach is now used. We assume that the restricted pool fraction can be divided into two pools, one of them fully saturated (Fig. 19). In order to calculate the steady state longitudinal magnetization and

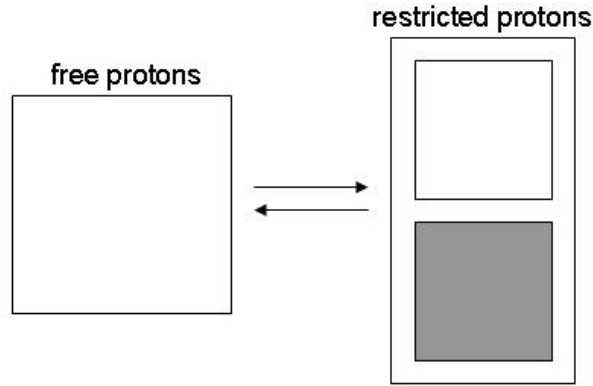


Figure 19: A simple MT model.

the saturation of the restricted pool we consider a spoiled gradient recalled (SPGR) echo method with short TR [8]. The longitudinal steady state magnetization is given by the Ernst equation

$$M_{ze} = \frac{M_0(1 - E_1)}{1 - E_1 \cos \alpha}. \quad (5.5)$$

From Eq. (5.1d)

$$M_{z,r} = M_{0,r} e^{-Wt}, \quad (5.6)$$

and, on the other hand, from SPGR

$$M_{z,r} = M_{0,r} \cos \alpha. \quad (5.7)$$

Thus, identifying $e^{-Wt} \equiv \cos \alpha$, we finally find

$$sat = 1 - \frac{1 - E_{1,r}}{1 - E_{1,r} \cos \alpha} = 1 - \frac{1 - E_{1,r}}{1 - E_{1,r} e^{-WT_{rf}}}. \quad (5.8)$$

Thus, the formula for the steady state magnetization described in the former section can be corrected by means of the saturation. Reducing the size of the fully saturated pool by a factor according to Eq. (5.8) yields an *MTR* curve showing a shape similar to measured data. We can observe a correction of the high *MTR* values for small flip angles. The maximal *MTR* is located at flip angles around 20° (Fig. 20). The maximal measured *MTR*-values, however, are achieved at flip angles around 50° (Fig. 15) and are considerably lower. Thus, the *MTR* values drop at high and low flip angles corresponding to measurements, while the maximum is not located at the expected flip angle. Furthermore, the simulated maxima have considerably higher values (*MTR* between 0.6 and 0.7) than the measured ones (*MTR* between 0.3 and 0.4).

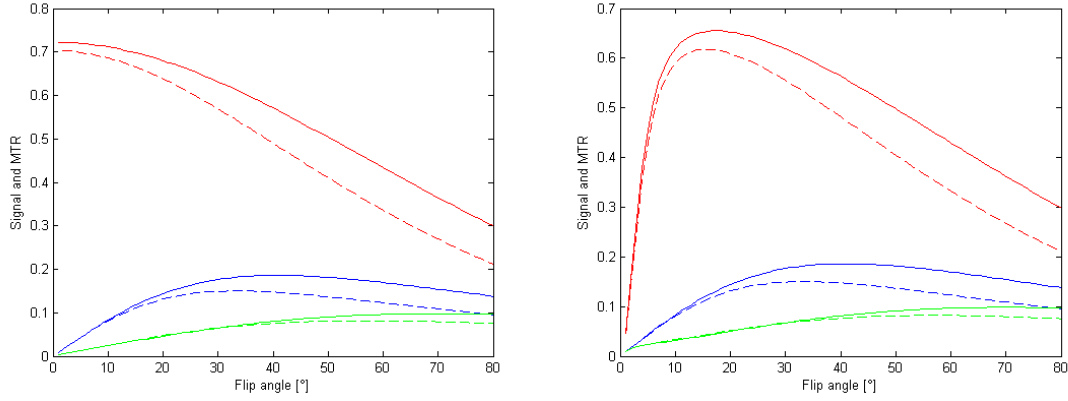


Figure 20: Signal behavior for the free pool (blue curve), for a fully saturated restricted pool (green curve) and *MTR* (red curve), for white and gray matter (solid and dashed lines, respectively). Left: calculated with one pool model, right: corrected by the saturation rate. $TR = 3$ ms, $T_{rf} = 640 \mu\text{s}$, $R_{1,f} = 1.71 \text{ s}^{-1}$, $T_{2,f} = 81$ ms for white matter, $R_{1,f} = 0.97 \text{ s}^{-1}$, $T_{2,f} = 93$ ms for gray matter, $R_{1,r} = 1 \text{ s}^{-1}$, $F = 0.157$ and $k_f = 4.45 \text{ s}^{-1}$.

6 Signal equation for the two pool model

6.1 Exchange matrix

Since the simple models did not lead to an appropriate description of tissue signals, we try to solve the two pool model equations. We therefore make an approximation which allows us to use a matrix formalism analogous to the one used in section 3.3.2. The approximation consists in separating relaxation and exchange between the two pools. In general, the magnetization vector is composed of four non-zero components: $\vec{M} = (M_{x,f} \ M_{y,f} \ M_{z,f} \ M_{z,r})$.

Eqs. (4.6a)-(4.6f) can be simplified by separating relaxation and exchange.

$$\frac{d\vec{M}}{dt} = \begin{pmatrix} 1 & 0 & 0 & 0 \\ 0 & 1 & 0 & 0 \\ 0 & 0 & -k_f & k_r \\ 0 & 0 & k_f & -k_r \end{pmatrix} \vec{M} = k_r \begin{pmatrix} 1 & 0 & 0 & 0 \\ 0 & 1 & 0 & 0 \\ 0 & 0 & F & 1 \\ 0 & 0 & F & -1 \end{pmatrix} \vec{M} \quad (6.1)$$

describes the exchange between the two pools, where $F = k_f/k_r$. This eigenvalue equation has the general solution $\vec{M}(t) = A(t) \cdot \vec{M}(0)$ with the exchange matrix

$$A(t) = \frac{1}{F+1} \begin{pmatrix} F+1 & 0 & 0 & 0 \\ 0 & F+1 & 0 & 0 \\ 0 & 0 & 1 + Fe^{-(F+1)k_r t} & 1 - e^{-(F+1)k_r t} \\ 0 & 0 & F(1 - e^{-(F+1)k_r t}) & F + e^{-(F+1)k_r t} \end{pmatrix}. \quad (6.2)$$

6.2 BSSFP signal with MT

To describe the bSSFP signal, i.e. the on-resonant case, with MT we consider the magnetization vector $\vec{M} = (M_{y,f} \ M_{z,f} \ M_{z,r})$. The exchange between the pools is given by

$$A(t) = \frac{1}{F+1} \begin{pmatrix} F+1 & 0 & 0 \\ 0 & 1 + Fe^{-(F+1)k_r t} & 1 - e^{-(F+1)k_r t} \\ 0 & F(1 - e^{-(F+1)k_r t}) & F + e^{-(F+1)k_r t} \end{pmatrix}. \quad (6.3)$$

The rotation matrix corresponding to the RF pulse is of form

$$R_x(\alpha) = \begin{pmatrix} \cos \alpha & \sin \alpha & 0 \\ -\sin \alpha & \cos \alpha & 0 \\ 0 & 0 & e^{-Wt} \end{pmatrix} \quad (6.4)$$

and contains the saturation of the bound pool. For alternating RF pulses, the rotation of the transverse magnetization about the z -axis is given by

$$R_z(\phi = 180^\circ) = \begin{pmatrix} -1 & 0 & 0 \\ 0 & 1 & 0 \\ 0 & 0 & 1 \end{pmatrix} \quad (6.5)$$

and the relaxation by

$$E = \begin{pmatrix} E_2 & 0 & 0 \\ 0 & E_{1,f} & 0 \\ 0 & 0 & E_{1,r} \end{pmatrix}, \quad (6.6)$$

where $E_2 = e^{-TR/T_{2,f}}$, $E_{1,f} = e^{-R_{1,f}TR}$ and $E_{1,r} = e^{-R_{1,r}TR}$.

The magnetization directly after the n -th RF pulse is $\vec{M}_n^+ = R_x \vec{M}_n^-$ and the signal directly before the $(n+1)$ -th pulse, assuming that relaxation and exchange can be separated, is

$$\vec{M}_{n+1}^- = A \left(E \vec{M}_n^+ + \vec{M}_0 \right). \quad (6.7)$$

For a steady state $\vec{M}_{n+1}^- = \vec{M}_n^-$ and thus

$$\vec{M}_n^- = \vec{M}_{n+1}^- = A \left(E R_x \vec{M}_n^- + \vec{M}_0 \right). \quad (6.8)$$

The eigenvalue equation takes the form

$$\vec{M}^+(\infty) = R_x [I - R_z A E R_x]^{-1} A \vec{M}_0 \quad (6.9)$$

in case the relaxation takes place before the exchange, where

$$\vec{M}_0 = \begin{pmatrix} 0 \\ M_{0,f}(1 - E_{1,f}) \\ M_{0,r}(1 - E_{1,r}) \end{pmatrix}. \quad (6.10)$$

In case the exchange takes place before the relaxation the signal directly before the $(n+1)$ -th pulse is given by

$$\vec{M}_{n+1}^- = E A \vec{M}_n^+ + \vec{M}_0 \quad (6.11)$$

and in the steady state

$$\vec{M}_n^- = \vec{M}_{n+1}^- = E A R_x \vec{M}_n^- + \vec{M}_0. \quad (6.12)$$

Thus, the eigenvalue equation is of form

$$\vec{M}^+(\infty) = R_x [I - R_z E A R_x]^{-1} \vec{M}_0. \quad (6.13)$$

As a reminder, the y -component of the bSSFP magnetization in the case without MT from Eq. (3.10) is

$$M_y^+(\infty) = M_0 \sin \alpha \frac{1 - E_1}{1 - E_1 E_2 - (E_1 - E_2) \cos \alpha}. \quad (6.14)$$

Eq. (6.9) can as well be solved analytically and yields the steady state MR signal M_y directly after the pulse.

$$M_y^+(\infty) = M_0 \sin \alpha \frac{(1 - E_{1,f})B + F(1 - E_{1,r})(1 - f_k)}{A - E_{1,f}E_2B - (E_{1,f}B - E_2A) \cos \alpha}, \quad (6.15)$$

where

$$A = 1 + F - F f_w E_{1,r} + f_k f_w E_{1,r}, \quad (6.16a)$$

$$B = 1 + F f_k - f_k f_w E_{1,r} + F f_k f_w E_{1,r}, \quad (6.16b)$$

$$f_k = e^{-(k_f + k_r)TR} =: e^{-kTR}, \quad (6.16c)$$

$$f_w = e^{-WT_{f}}, \quad (6.16d)$$

$M_{0,f} = 1$, $M_{0,r} = F M_{0,f}$, $E_2 = e^{-TR/T_{2,f}}$, $E_{1,f} = e^{-R_{1,f}TR}$ and $E_{1,r} = e^{-R_{1,r}TR}$. The signal achieved at the echo time TE reads

$$M_y(TE) = \sqrt{E_2} M_y^+(\infty). \quad (6.17)$$

The limit of a vanishing restricted pool, i.e. $F \rightarrow 0$, $k \rightarrow 0$, $W \rightarrow 0$ and $E_{1,r} \rightarrow 0$, gives us $f_k \rightarrow 1$, $f_w \rightarrow 1$, $A \rightarrow 1$ and $B \rightarrow 1$, which lets the solution converge towards the well-known bSSFP solution without MT.

Fig. 21 shows the dependency of the calculated curves on the flip angle, where formula (6.15) is used. The case where relaxation takes place before exchange as well as the case where exchange takes place before relaxation are depicted. All the curves are valid for white brain matter, using $TR = 3$ ms and $T_{rf} = 640$ μ s. This result corresponds well

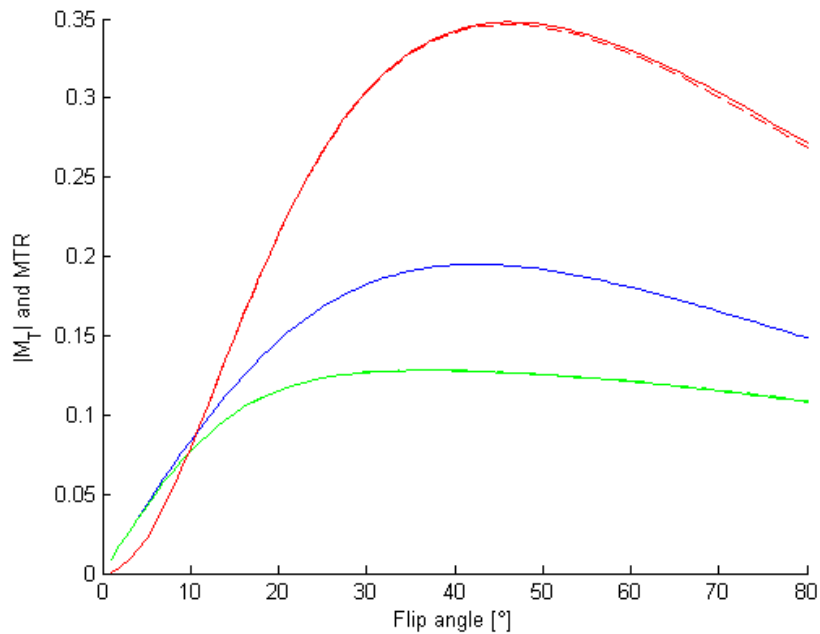


Figure 21: Calculated bSSFP signal and MTR as a function of α for white brain matter. Blue curve: signal without MT. Green curve: signal with MT. Red curve: MTR . Relaxation before exchange (solid lines) and exchange before relaxation (dashed lines). $TR = 3$ ms, $T_{rf} = 640$ μ s, $R_{1,f} = 1.71$ s $^{-1}$, $T_{2,f} = 81$ ms, $R_{1,r} = 1$ s $^{-1}$, $F = 0.157$ and $k_f = 4.45$ s $^{-1}$.

to the measured data (Fig. 15). In Fig. 22, we see the behavior of the signal and the MTR curves as a function of TR , where formula (6.15) was used. In the case without MT, W was set to zero. The same three curves are depicted in dependency of k_f in Fig. 22. All curves were calculated for $\alpha = 40^\circ$. After including the magnetization transfer we thus get the bSSFP signal dependency on TR which corresponds to the measured values (Fig. 23), i.e. a considerable signal increase instead of a constant signal as seen in Eq. (3.11).

By extrapolating the MTR signal for $TR \rightarrow 0$ the situation of infinitely many RF pulses per second is achieved and therefore full saturation occurs (section 5.1). Then $M_{z,r}$ equals zero, which allows a high transfer from $M_{z,f}$ to $M_{z,r}$. Thus, the signal $M_{y,f}$ is relatively low whereas the MTR signal is high. By this means, we get $MTR = 0.57$ for $TR = 0$. On the other hand Fig. 22 enables us to read the rate k_f for $MTR = 0.57$, what leads to $k_f = 4.5$. Theoretically, it is thus possible to determine the rate k_f from the MTR value by extrapolation. However, it turns out not to be a practical method because the lowest possible TR lies around 2.9 ms. In the applicable TR region the characteristic turn of the

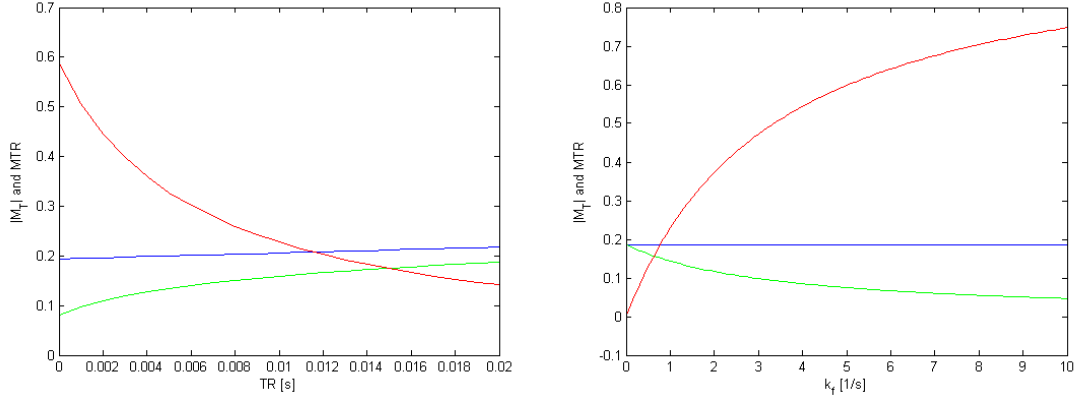


Figure 22: BSSFP signal (blue curve: without MT, green curve: with MT) and MTR (red curve) dependency on TR and k_f . $R_{1,f} = 1.71 \text{ s}^{-1}$, $T_{2,f} = 81 \text{ ms}$, $R_{1,r} = 1 \text{ s}^{-1}$ and $F = 0.157$. $k_f = 4.45 \text{ s}^{-1}$ for the TR dependency. $TR = 1 \text{ ms}$ and $T_{rf} = 640 \text{ }\mu\text{s}$ for the k_f dependency.

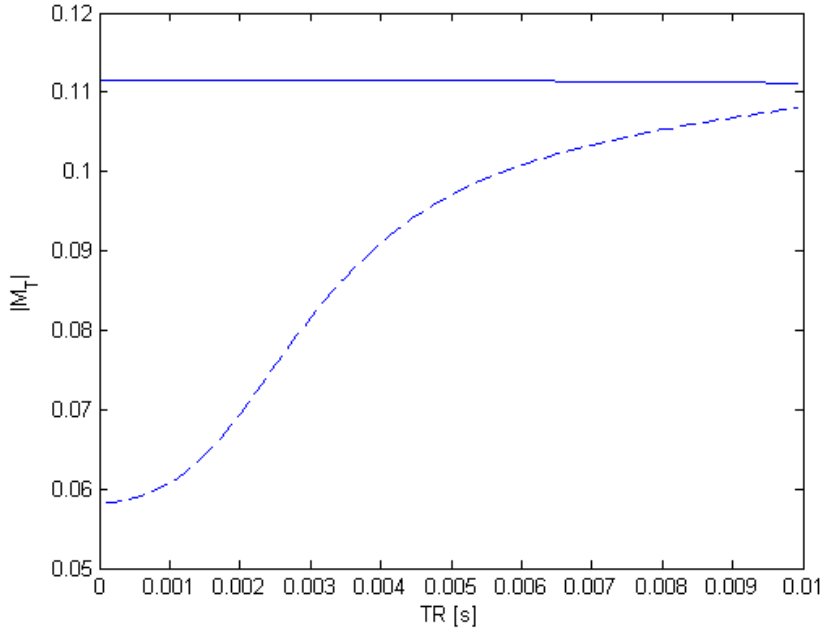


Figure 23: BSSFP signal dependency on TR . Theoretical curve without MT (solid line) and with MT (dashed line) for white brain matter. $R_{1,f} = 1.71 \text{ s}^{-1}$, $R_{1,r} = 1 \text{ s}^{-1}$, $T_{2,f} = 40 \text{ ms}$, $\alpha = 50^\circ$, $F = 0.157$ and $k_f = 4.45 \text{ s}^{-1}$.

signal curve towards saturation (for $TR \rightarrow 0$) can not be measured. In addition to the signal curves as a function of TR for $T_{rf} = 270 \mu\text{s}$, the curves as a function of TR for a varying T_{rf} are depicted in Fig. 24.

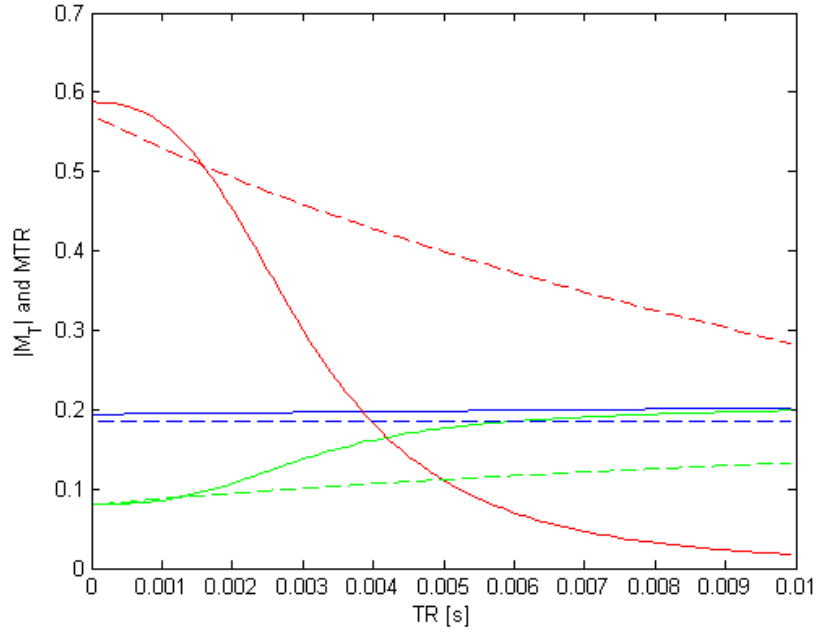


Figure 24: BSSFP signal (blue curve: without MT, green curve: with MT) and MTR (red curve) dependency on TR . Dashed lines: constant T_{rf} , solid lines: varying T_{rf} . $R_{1,f} = 1.71 \text{ s}^{-1}$, $T_{2,f} = 81 \text{ ms}$, $R_{1,r} = 1 \text{ s}^{-1}$, $F = 0.157$ and $k_f = 4.45 \text{ s}^{-1}$.

7 Materials and methods

7.1 Experimental basics

An MR tomograph basically consists of superconducting coils to generate the main magnetic field B_0 , a transmitting unit, a receiving unit, a computer for the handling and a unit for signal processing and image reconstruction (Fig. 25). For examinations the patient

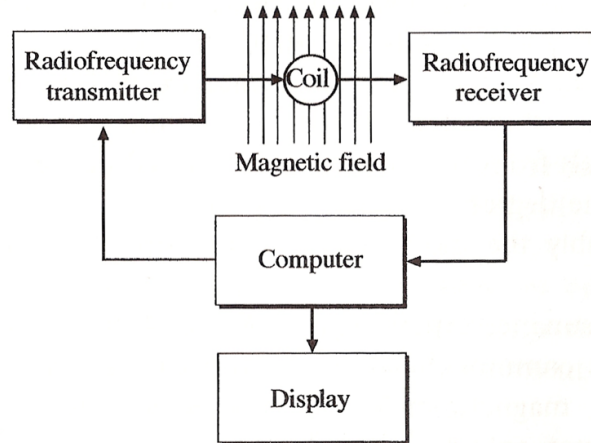


Figure 25: Basic components of an MR tomograph [1].

lies in a tube surrounded by the magnetic coils. The latter are usually located in a bath of liquid helium at 4 K, in which they become superconducting. Apart from the main magnetic coils, there are insulating layers, gradient coils and shimming coils around the tube. The purpose of the shimming coils is to homogenize the main magnetic field before a measurement is initiated.

An RF synthesizer generates RF pulses of a given phase and duration whereas a modulator is responsible for the requested pulse shape. Depending on the flip angle and the sample the amplifier provides pulses of a specific voltage amplitude. Before applying pulses, they are compared to a reference in order to prevent tissue damages. The power irradiation for imaging humans must not exceed 4 W/kg. The receiving coils are shaped according to the examination region. Finally, the received signal is fed via a preamplifier to a recording computer.

7.2 Measurements and postprocessing

All our MR imaging experiments were performed using a Siemens Avanto 1.5 T scanner (Fig. 26). The voxel size was $1.33 \times 1.33 \times 1.33 \text{ mm}^3$. The 3D measurements with a matrix of $144 \times 192 \times 192$ pixels consisted of

- an MPRAGE sequence yielding a good contrast between gray and white matter and being used for segmentation,
- two SPGR echos with $\alpha = 4^\circ$ and $\alpha = 15^\circ$, respectively, for the calculation of a T_1 map,



Figure 26: MR tomograph Siemens Avanto 1.5 T.

- 8 bSSFP (TrueFISP) sequences with different repetition times and
- 8 bSSFP (TrueFISP) sequences with different flip angles.

The first 8 bSSFP measurements at a flip angle of 35° were performed with the following repetition times and RF pulse durations:

TR [ms]	2.92	2.99	3.09	3.26	3.52	3.88	4.28	4.78
T_{rf} [μ s]	230	300	400	580	840	1200	1600	2100

The second 8 bSSFP sequences were measured at $TR = 2.99$ ms, $T_{rf} = 270$ μ s and these flip angles:

Flip angle [$^\circ$]	5	10	15	20	25	30	35	40
-------------------------	---	----	----	----	----	----	----	----

A manual shim was carried out before these 16 measurements. The whole data acquisition takes about thirty minutes. The bSSFP sequence is preferred to the SSFP sequence since the latter is prone to flow artifacts. In order to compensate for motion artifacts, the data sets are segmented by separating the skull from the brain and registered. The original data are converted to NIFTI data sets, which can be edited using MATLAB.

7.3 T_1 maps

Longitudinal relaxation times T_1 of the free pool were derived based on the DESPOT1 method [19]. According to Eq. (2.19) the z -magnetization can be written as

$$M_z(t) = M_z(0)E_1 + M_0(1 - E_1). \quad (7.1)$$

This can be related to the signal intensity S by

$$\frac{S}{\sin \alpha} = \frac{S}{\tan \alpha} E_1 + M_0(1 - E_1). \quad (7.2)$$

Eq. (7.2) is of form $y = mx + b$. If we plot $S/\sin \alpha$ versus $S/\tan \alpha$ we get the slope $m = e^{-TR/T_1}$. Two signal measurements S_1 and S_2 yield the slope

$$m = \frac{S_2/\sin \alpha - S_1/\sin \alpha}{S_2/\tan \alpha - S_1/\tan \alpha}. \quad (7.3)$$

Hence, we can calculate the longitudinal relaxation time by

$$T_1 = -\frac{TR}{\ln m}. \quad (7.4)$$

Using this method, only two flip angle measurements are required to obtain $T_{1,f}$. The longitudinal relaxation time of the restricted pool $T_{1,r}$ is not determined by MT experiments. In our parameter estimations, it is set to the same value as for the free pool, $R_{1,r} = R_{1,f}$, whereas other experiments were performed with $R_{1,r} = 1 \text{ s}^{-1}$ cf. [18].

7.4 Parameter estimations

Knowing the bSSFP signal dependency on the repetition time and the flip angle, based on Eq. (6.15), it is possible to estimate several parameters of the two pool model. One alternative consists in fitting the MTR signal as a function of the flip angle. Therefore, TR , T_{rf} , T_1 , $T_{2,f}$ and W are held constant. The flip angle is varied and the parameters $k = k_f + k_r$ and $F = k_f/k_r$ as well as the amplitude are estimated by the least squares method. This fit is very sensitive to $T_{2,f}$.

Another alternative is to fit the steady state signal as a function of the repetition time. Here, α , T_1 and $T_{2,f}$ are given and W is calculated for every TR , RF pulse duration and RF pulse shape. The repetition time and simultaneously the pulse duration are varied and the parameters k and F as well as the amplitude are estimated. This method is very sensitive to the semisolid pool fraction F and the exchange rate k .

By means of a global fit over all flip angles and all TR , not only k , F and the amplitude, but also $T_{2,f}$ can be reliably received. From k and F follow $k_f = kF/(F + 1)$ and $k_r = k/(F + 1)$. The fitting procedure can be applied to every voxel of the MR image. Hence, an intensity distribution for the parameters F , k_f and $T_{2,f}$ can be depicted. This leads to a parameter map of a transverse brain slice or a three dimensional map of the whole brain containing the quantitative model parameters. The fitting process uses the same initial values for white and gray brain matter, but different ones for CSF. The choice of initial values is made on the basis of the bSSFP signal strength of the $\alpha = 40^\circ$ image for each voxel. If white or gray matter is selected, the two pool model formula, Eq. (6.15), is used for the fit. In case no solution is found and in case CSF is detected, the one pool model equation, Eq. (3.11), is applied.

8 Results

8.1 Numerical simulation

A numerical simulation of the system of differential equations (4.6a)-(4.6f) is performed to justify the simplification of separating relaxation and exchange. We use an explicit Runge-Kutta (4,5) formula for the numerical simulation of the steady state signal for a given flip angle. After the steady state is reached, the signal is read out at $TE = TR/2$. This is shown for white matter, for $\alpha = 40^\circ$, $W = 0$, $TR = 6$ ms, $T_{rf} = 2700$ μ s and 1000 simulation steps in Fig. 27. Figures 28 and 29 display a comparison of the numerical

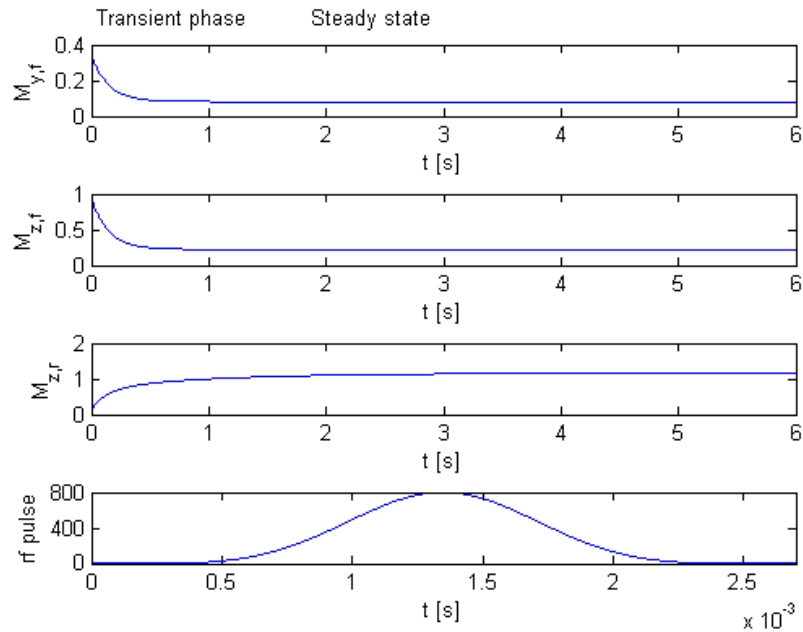


Figure 27: Development of $M_{y,f}$, $M_{z,f}$ and $M_{z,r}$ for a bSSFP sequence after irradiation of an RF pulse until the steady state is reached. $\alpha = 40^\circ$, $W = 0$, $TR = 6$ ms, $T_{rf} = 2700$ μ s, 1000 simulation steps, $R_{1,f} = 1.71$ s^{-1} , $T_{2,f} = 81$ ms, $R_{1,r} = 1$ s^{-1} , $F = 0.157$ and $k_f = 4.45$ s^{-1} .

solution (3000 simulation steps) with the analytical solution for white matter. It can be found that the case of relaxation before exchange yields a calculated MTR signal which is only 0.43 % higher than in the case of exchange before relaxation. For $W = 0$ both cases lead to the same signal whereas for $W \neq 0$ the case of relaxation before exchange leads to a lower signal. For long pulse durations we observe that the simulated MT signal values are slightly higher than the calculated ones. In this case the calculation produces a bigger error because we assume an instantaneous rotation caused by an infinitesimally short pulse. If this were true, M_T would immediately be built up and the signal is strongly reduced by relaxation. In reality (simulation), however, M_T is slowly built up, whereby the relaxation does not influence the maximal transverse magnetization all the time, leading to a higher signal at TR .

The difference between simulation and calculation (exchange before relaxation) at a flip angle of 40° amounts to 1.5 % for white matter and to 2.5 % for gray matter. Thus,

the analytical formula describes the signal behavior adequately and can be used for fits of measured data.

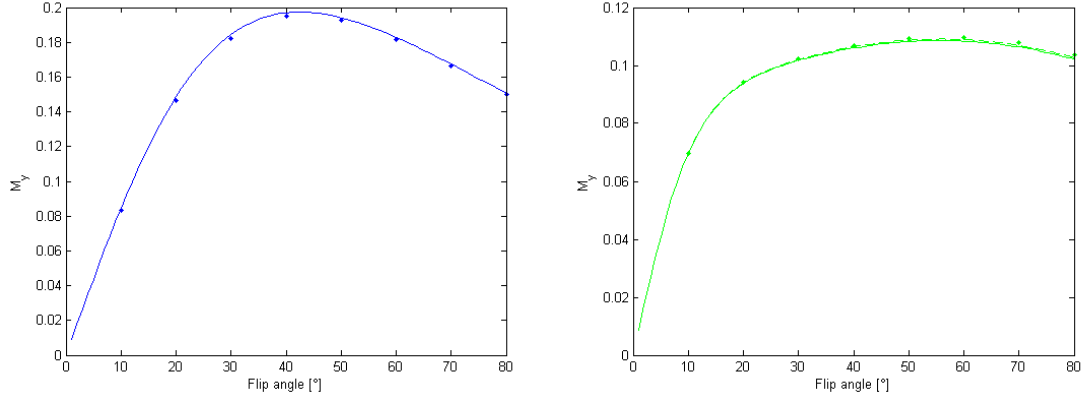


Figure 28: Numerical signal simulation of the exact equations (dots) compared to the analytical solution (solid line) without MT (left) and with MT (right) (solid line: relaxation before exchange, dashed line: exchange before relaxation). $R_{1,f} = 1.71 \text{ s}^{-1}$, $T_{2,f} = 81 \text{ ms}$, $R_{1,r} = 1 \text{ s}^{-1}$, $F = 0.157$ and $k_f = 4.45 \text{ s}^{-1}$. $TR = 6 \text{ ms}$, $T_{rf} = 2700 \text{ }\mu\text{s}$ in the case without MT, $TR = 3.5 \text{ ms}$, $T_{rf} = 340 \text{ }\mu\text{s}$ in the case with MT.

8.2 Parameter images

First, a magnetization prepared rapid gradient echo (MPRAGE) is acquired. Based on this image a segmentation of the whole 3D data set is performed. The segmented image shows a good contrast between white and gray matter (Fig. 30). Secondly, two SPGR echos are acquired with flip angles $\alpha = 4^\circ$ and $\alpha = 15^\circ$ (Fig. 31). These two images are used to calculate a T_1 map based on the DESPOT1 method (Fig. 32). Furthermore, 16 bSSFP images are acquired, yielding different signal strengths depending on α and TR , respectively (Fig. 32). The fitting procedure based on the 16 segmented images is then applied.

Examples of one point global fits for white and gray matter, respectively, can be seen in Fig. 33 and Fig. 34. The global fit yields parameter estimates for F , k_f and $T_{2,f}$. Applying the global fit to every pixel of one brain slice results in parameter images. As the fractional pool size is correlated with myelin, F has higher values in white matter than in gray matter. The fitted exchange rate k_f yields an image contrast similar to F as can be seen from the slice fit in Fig. 35. The fitted $T_{2,f}$ images show the same contrast as usual T_2 -weighted scans (Fig. 36).

To compare fitted values in different subjects, two of the regions of interest (ROI) displayed in Fig. 37 were selected. The parameters resulting from acquisitions in two healthy volunteers are displayed in Table 1. The white matter regions for both subjects

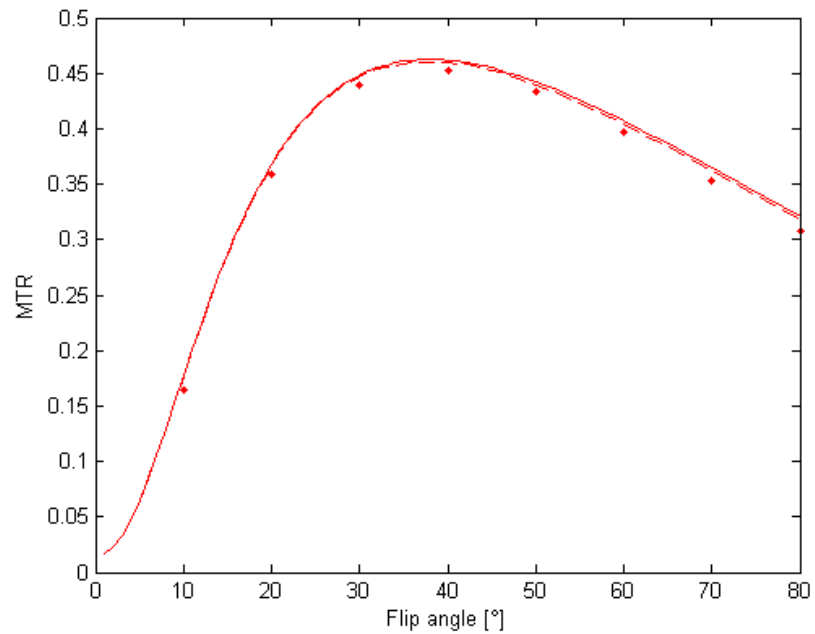


Figure 29: Numerical *MTR* simulation of the exact equations (dots) compared to the analytical solution (solid line: relaxation before exchange, dashed line: exchange before relaxation). $R_{1,f} = 1.71 \text{ s}^{-1}$, $T_{2,f} = 81 \text{ ms}$, $R_{1,r} = 1 \text{ s}^{-1}$, $F = 0.157$ and $k_f = 4.45 \text{ s}^{-1}$. $TR = 6 \text{ ms}$, $T_{rf} = 2700 \text{ }\mu\text{s}$ in the case without MT, $TR = 3.5 \text{ ms}$, $T_{rf} = 340 \text{ }\mu\text{s}$ in the case with MT.

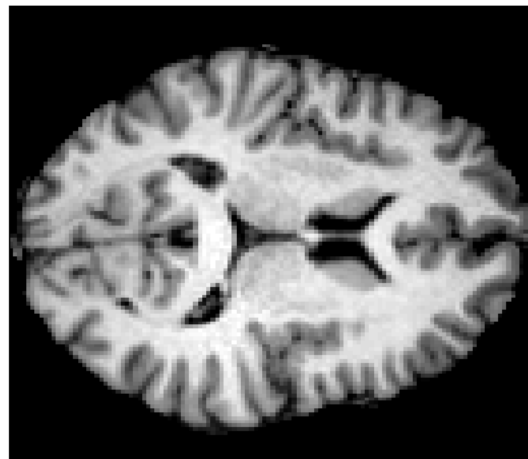


Figure 30: Segmented MPRAGE image showing a good contrast between white and gray matter.

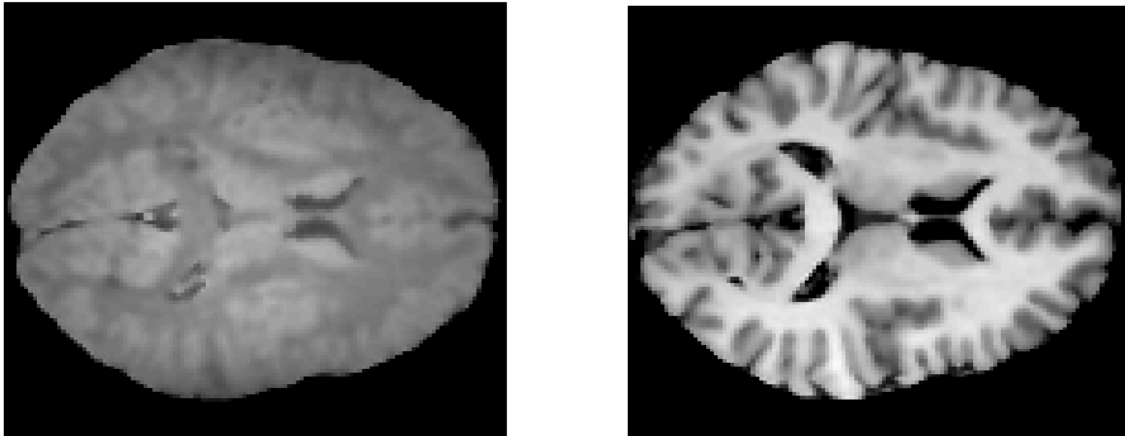


Figure 31: SPGR images with flip angles $\alpha = 4^\circ$ and $\alpha = 15^\circ$.

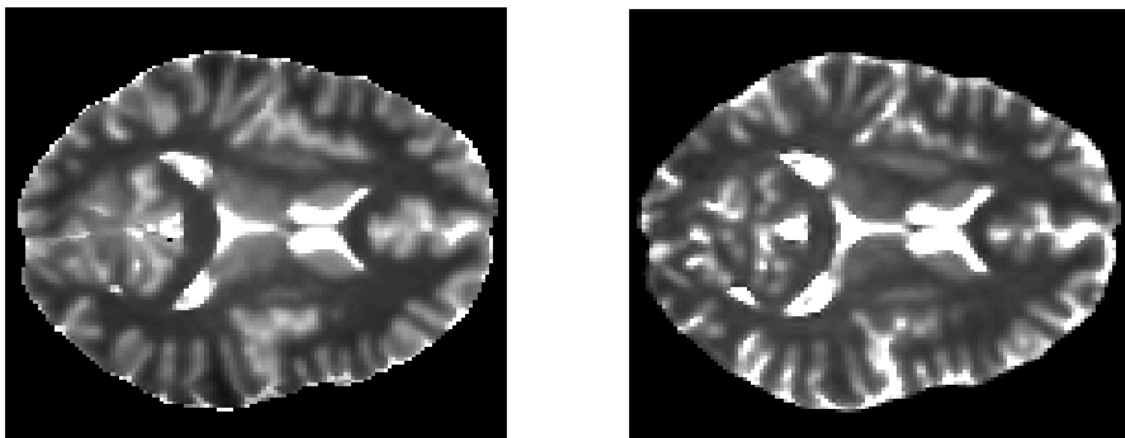


Figure 32: T_1 map calculated with the DESPOT1 method (left) and bSSFP image with $TR = 2.92$ ms and $T_{rf} = 230$ μ s.

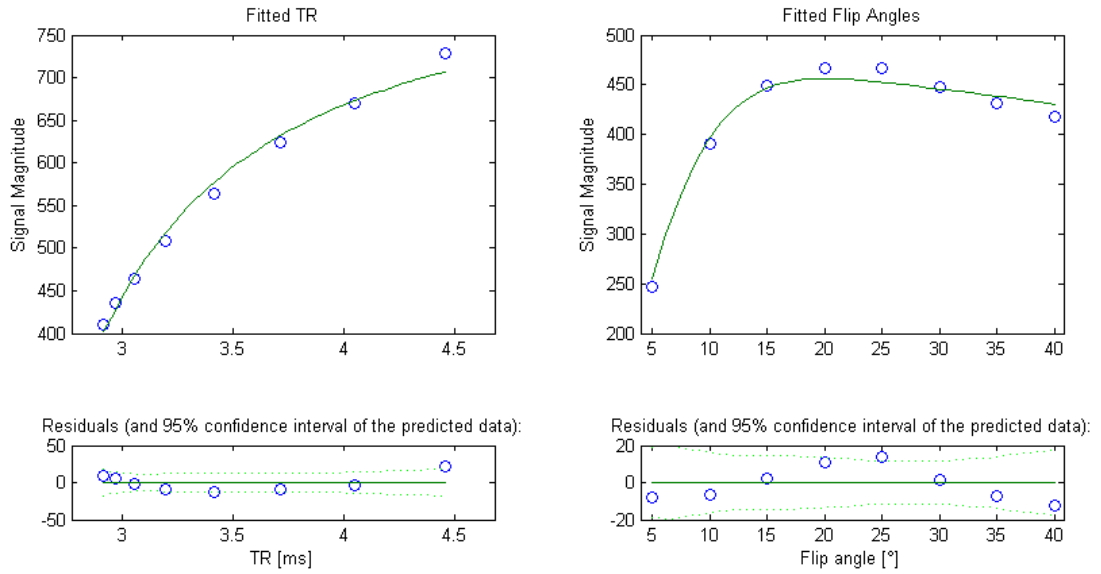


Figure 33: Example of a one point global fit for white brain matter yielding the parameter estimates $F = 16.6 \pm 6.2 \%$, $k_f = 6.1 \pm 3.0 \text{ s}^{-1}$ and $T_{2,f} = 43.4 \pm 8.7 \text{ ms}$.

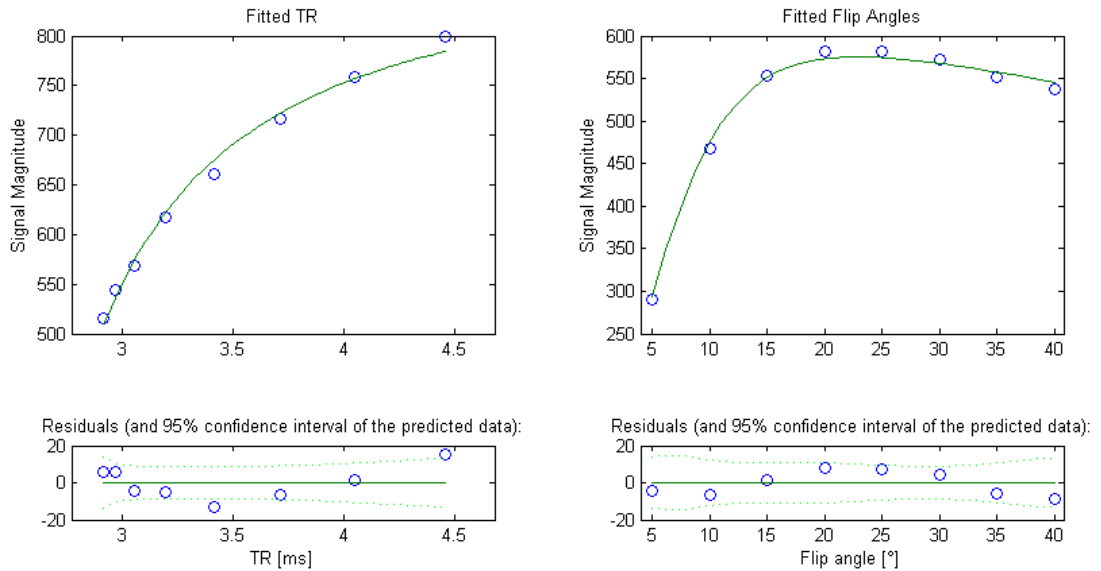


Figure 34: Example of a one point global fit for gray brain matter yielding the parameter estimates $F = 7.6 \pm 2.0 \%$, $k_f = 2.9 \pm 1.1 \text{ s}^{-1}$ and $T_{2,f} = 63.9 \pm 7.3 \text{ ms}$.

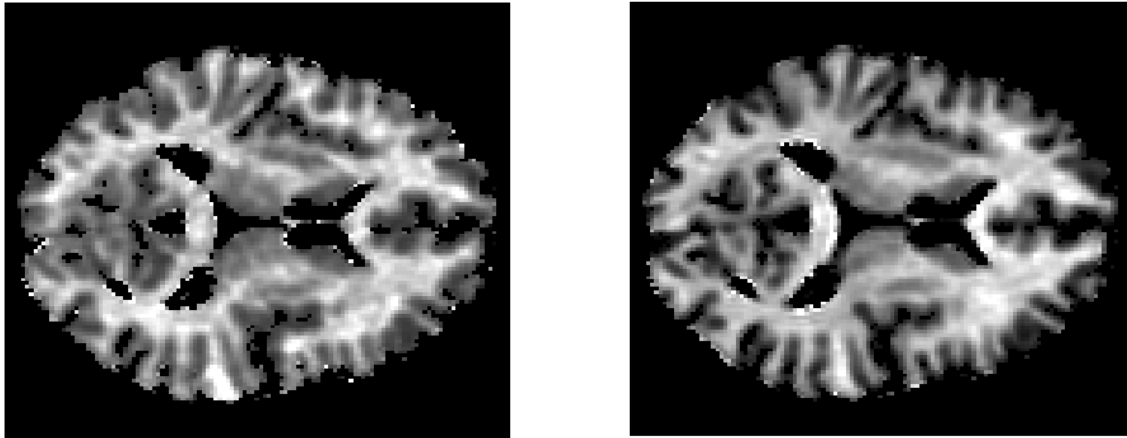


Figure 35: Example of a slice fit showing parameter estimates for F (left) and k_f (right).

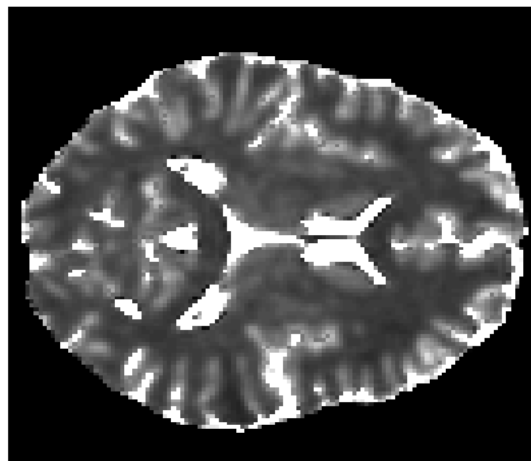


Figure 36: Example of a slice fit showing parameter estimates for $T_{2,f}$.

were selected from the corpus callosum splenium whereas the gray matter regions were selected from the caudate nucleus.

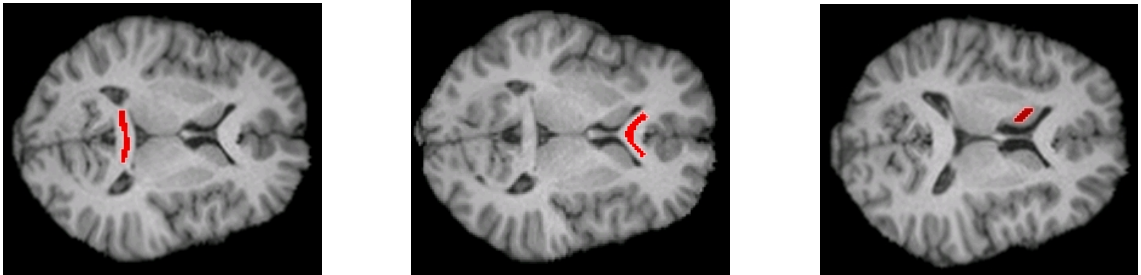


Figure 37: Selected regions for the stability analysis: corpus callosum splenium (left) and corpus callosum genu (middle) for white matter and caudate nucleus (right) for gray matter.

	Subject 1		Subject 2	
	White matter	Gray matter	White matter	Gray matter
F [%]	15.1 ± 1.3	6.8 ± 0.7	16.3 ± 2.6	7.1 ± 0.8
k_f [s^{-1}]	6.3 ± 0.9	2.8 ± 0.4	6.1 ± 1.2	2.6 ± 0.3
$T_{1,f}$ [ms]	756 ± 23	$1199 \pm 69 \pm 76$	780 ± 81	1134 ± 65
$T_{2,f}$ [ms]	46 ± 4	67 ± 5	47 ± 6	67 ± 6
MTR [%]	43.6 ± 1.2	34.8 ± 1.6	43.1 ± 1.5	33.6 ± 1.4

Table 1: Parameter estimates for F , k_f and $T_{2,f}$ and measurements of $T_{1,f}$ and MTR for two selected regions in two healthy volunteers. Values for white matter were derived from corpus callosum splenium and values for gray matter from caudate nucleus.

9 Discussion of the results

9.1 Comparison with literature values

Sled and Pike [18] described an imaging technique that yields the parameters of a two pool model for magnetization transfer. Spoiled gradient echo sequences in which shaped off-resonance pulses were interleaved with small angle on-resonance excitation pulses were used. For one in vivo experiment 60 MT-weighted images and B_1 , B_0 , T_1 and T_2 maps were acquired within 35 minutes. Thereafter, each scan was analyzed using a closed form expression for the signal to yield parameter images for the model parameters.

The average regional parameters resulting from our method based on bSSFP are compared to the literature values (Tab. 2). The bound proton fraction F corresponds very well for white matter whereas for gray matter it lies 25 % above the literature value. Our exchange rates k are 44 % and 32 % higher than literature values for white and gray matter, respectively. For the relaxation time T_1 discrepancies of 30 % and 16 %, for T_2 discrepancies of 29 % and 22 % for white and gray matter, respectively, are observed. Reasons for the discrepancies between our parameters and the literature values may be different approaches concerning the exchange rate $R_{1,r}$ and the absorption line shape $G(\Delta)$.

	WM lit.	GM lit.	WM reg.	GM reg.	WM seg.	GM seg.
F [%]	15.7	5.6	15.5	7.0	14.4	7.0
k_f [s^{-1}]	4.5	2.2	6.5	2.9	5.5	2.7
$T_{1,f}$ [ms]	556	1010	723	1170	774	1100
$T_{2,f}$ [ms]	34	55	44	67	48	83

Table 2: Parameter estimates of F , k_f and $T_{2,f}$ and measurements of $T_{1,f}$ based on bSSFP compared to literature values [18]. Values for white matter were derived from corpus callosum splenium and values for gray matter from caudate nucleus. Literature values (left), average estimates in the same region of interest (middle) and average segmentation values (right).

All data was acquired using a 1.5 T MRI system. In our study the voxel size was $1.33 \times 1.33 \times 1.33 \text{ mm}^3$ whereas for the cited values the in-plane resolution was 2 mm and the slice thickness 7 mm. In addition to higher resolution our acquisition time was substantially shorter, allowing 3D instead of 2D data sets within about 30 minutes.

9.2 Fitting sensitivities and off-resonance effects

It turns out that the line shape $G = G(\Delta)$, which determines the mean saturation rate of the restricted pool, Eq. (4.4), strongly influences the fitted values. The frequency offset Δ can not be varied and it is not possible to determine the exact value of G . Since the exact value is not known, we tried to include it in the global fit. This, however, lead to a ten times smaller G than expected. Therefore, we fixed it at $G = 1.4 \cdot 10^{-5} \text{ s}^{-1}$. It is not clear whether the line shape should be varied for different types of brain tissue.

Assuming the effective flip angle does not exactly correspond to the chosen one, the fitted parameters also change. The changes in F , k , k_r and $T_{2,f}$ are of the same magnitude as the flip angle deviation whereas the change in k_f is smaller. In the future, a quantitative

B_1 map could be acquired to examine spatial variations of the applied RF pulses and, if necessary, correct the flip angles throughout the image.

Magnetic field inhomogeneities lead to small off-resonance dephasing angles ϕ . To study the off-resonance behavior the signal was simulated with and without saturation as a function of ϕ (Fig. 38). The signals and the difference of the two signals are approximately constant in the region of on-resonance.

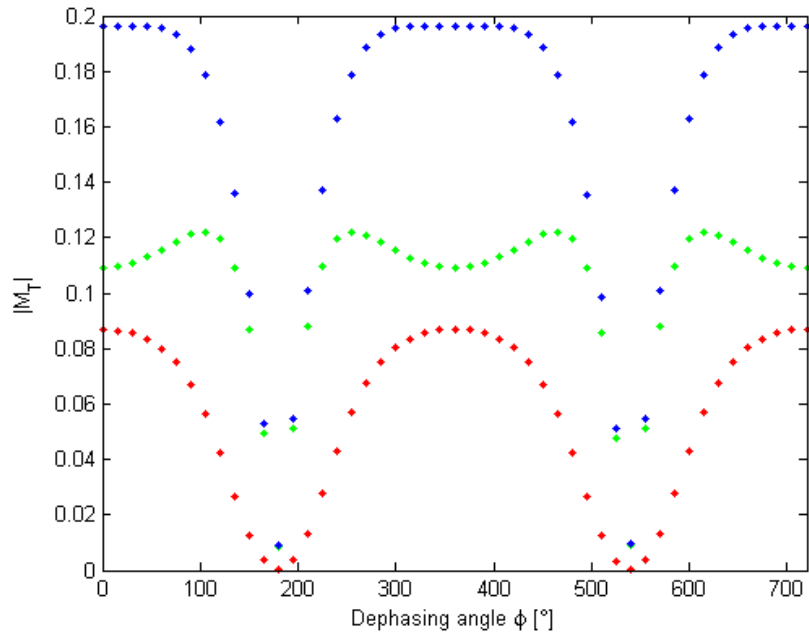


Figure 38: Off-resonance simulation for white matter, $TR = 3.5$ ms, $T_{rf} = 340$ μ s and $\alpha = 40^\circ$. Blue curve: signal without saturation, green curve: signal with saturation, red curve: difference of the two signals.

9.3 Stability analysis

In order to analyze the stability of the fitted and measured parameters, five acquisitions with the same volunteer were performed with a time-lag of one to three weeks. Parameter estimates derived from corpus callosum genu and corpus callosum splenium for white matter and from caudate nucleus for gray matter (Fig. 37) are shown in Tables 3 to 5. Furthermore, a 3D segmentation of white and gray matter based on an MPRAGE image yields the parameters in Tables 6 and 7. All the parameters seem to be stable over time, both for a selected region and a 3D segmentation of the whole brain. Differences in the ROI analysis may result from slightly different selected regions and volunteer positions. The segmentation values depend strongly on the selected limits between white and gray matter in the MPRAGE image. What stands out is that the exchange rate k_f is higher in the caudate nucleus genu than in the caudate nucleus splenium whereas the relaxation times are lower.

	WM 1	WM 2	WM 3	WM 4	WM 5	Average
F [%]	16.7 ± 1.4	17.0 ± 1.7	17.0 ± 1.7	17.0 ± 1.4	16.8 ± 1.6	16.9 ± 0.7
k_f [s^{-1}]	8.6 ± 0.8	8.5 ± 0.7	8.7 ± 0.9	8.5 ± 0.7	8.7 ± 0.8	8.6 ± 0.4
$T_{1,f}$ [ms]	654 ± 25	675 ± 30	657 ± 25	650 ± 25	642 ± 27	656 ± 12
$T_{2,f}$ [ms]	38 ± 2	37 ± 2	36 ± 2	37 ± 3	38 ± 2	37 ± 1
MTR [%]	44.3 ± 0.7	44.8 ± 1.3	44.6 ± 1.2	43.8 ± 1.4	44.7 ± 1.1	44.4 ± 0.5

Table 3: Parameter fits of F , k_f and $T_{2,f}$ and measurements of $T_{1,f}$ and MTR for white matter, corpus callosum genu.

	WM 1	WM 2	WM 3	WM 4	WM 5	Average
F [%]	15.4 ± 1.4	15.3 ± 1.5	15.7 ± 1.6	15.6 ± 1.3	15.4 ± 1.8	15.5 ± 0.7
k_f [s^{-1}]	6.7 ± 0.7	6.3 ± 0.5	6.8 ± 0.6	6.3 ± 0.7	6.6 ± 0.7	6.5 ± 0.3
$T_{1,f}$ [ms]	744 ± 21	719 ± 15	725 ± 21	715 ± 22	718 ± 23	723.2 ± 9.3
$T_{2,f}$ [ms]	44 ± 2	44 ± 2	41 ± 3	45 ± 3	46 ± 3	44 ± 1
MTR [%]	43.8 ± 1.7	42.6 ± 1.9	43.5 ± 1.1	42.6 ± 1.4	43.3 ± 1.5	43.2 ± 0.7

Table 4: Parameter fits of F , k_f and $T_{2,f}$ and measurements of $T_{1,f}$ and MTR for white matter, rear corpus callosum.

	GM 1	GM 2	GM 3	GM 4	GM 5	Average
F [%]	7.1 ± 1.1	6.9 ± 0.5	7.1 ± 1.0	6.8 ± 0.9	6.9 ± 0.7	7.0 ± 0.4
k_f [s^{-1}]	2.9 ± 0.5	2.9 ± 0.5	2.9 ± 0.2	2.8 ± 0.5	2.9 ± 0.4	2.9 ± 0.2
$T_{1,f}$ [ms]	1175 ± 95	1180 ± 67	1178 ± 82	1165 ± 108	1156 ± 79	1170 ± 39
$T_{2,f}$ [ms]	66 ± 6	68 ± 5	64 ± 5	68 ± 5	67 ± 4	67 ± 2
MTR [%]	35.2 ± 1.8	35.0 ± 1.8	35.4 ± 0.8	34.4 ± 1.9	33.8 ± 2.9	34.8 ± 0.9

Table 5: Parameter fits of F , k_f and $T_{2,f}$ and measurements of $T_{1,f}$ and MTR for gray matter, caudate nucleus.

	WM 1	WM 2	WM 3	WM 4	WM 5	Average
F [%]	14.5 ± 3.0	14.2 ± 3.1	14.7 ± 3.1	14.4 ± 3.0	14.2 ± 3.1	14.4 ± 1.4
k_f [s^{-1}]	5.5 ± 1.2	5.4 ± 1.2	5.5 ± 1.2	5.7 ± 1.3	5.8 ± 1.2	5.5 ± 0.5
$T_{1,f}$ [ms]	775 ± 108	780 ± 117	778 ± 117	776 ± 119	760 ± 113	774 ± 51
$T_{2,f}$ [ms]	48 ± 9	49 ± 10	47 ± 9	49 ± 10	49 ± 12	48 ± 5
MTR [%]	41.5 ± 3.4	41.3 ± 3.5	41.4 ± 3.2	41.3 ± 3.5	41.5 ± 3.8	41.4 ± 1.6

Table 6: Parameter fits of F , k_f and $T_{2,f}$ and measurements of $T_{1,f}$ and MTR for white matter, 3D segmentation.

	GM 1	GM 2	GM 3	GM 4	GM 5	Average
F [%]	7.3 ± 3.8	6.9 ± 3.8	7.1 ± 3.9	6.9 ± 3.8	6.8 ± 3.5	7.0 ± 1.7
k_f [s^{-1}]	2.7 ± 1.5	2.6 ± 1.5	2.6 ± 1.6	2.5 ± 1.5	2.9 ± 1.5	2.7 ± 0.7
$T_{1,f}$ [ms]	1100 ± 263	1113 ± 282	1103 ± 286	1106 ± 290	1079 ± 292	1100 ± 126.5
$T_{2,f}$ [ms]	77 ± 51	84 ± 60	83 ± 64	87 ± 66	83 ± 58	83 ± 27
MTR [%]	32.7 ± 8.1	32.5 ± 8.2	32.5 ± 8.3	32.2 ± 8.4	31.9 ± 8.6	32.4 ± 3.7

Table 7: Parameter fits of F , k_f and $T_{2,f}$ and measurements of $T_{1,f}$ and MTR for gray matter, 3D segmentation.

9.4 Issues

The bSSFP sequence is sensitive to off-resonance effects. Using a manual shimming procedure a frequency of $\nu \approx 20$ Hz is achieved. This frequency corresponds to a magnetic field inhomogeneity of $2\pi\nu/(\gamma B_0) \approx 0.31$ ppm. The resulting off-resonance dephasing angle amounts to $\Delta\phi = \pm 9^\circ$. According to the off-resonance simulation (Fig. 38, signal with saturation) a variation of $\pm 15^\circ$ in ϕ leads to a signal difference of approximately ± 0.4 %. Thus, with a good shim nearly negligible off-resonance effects can be achieved.

Even with a good shim, large local field variations may occur in the outer brain regions. At certain off-resonance frequencies the signal disappears entirely and bands of signal loss, i.e. banding artifacts, appear (Fig. 39). Such banding artifacts can be strongly reduced

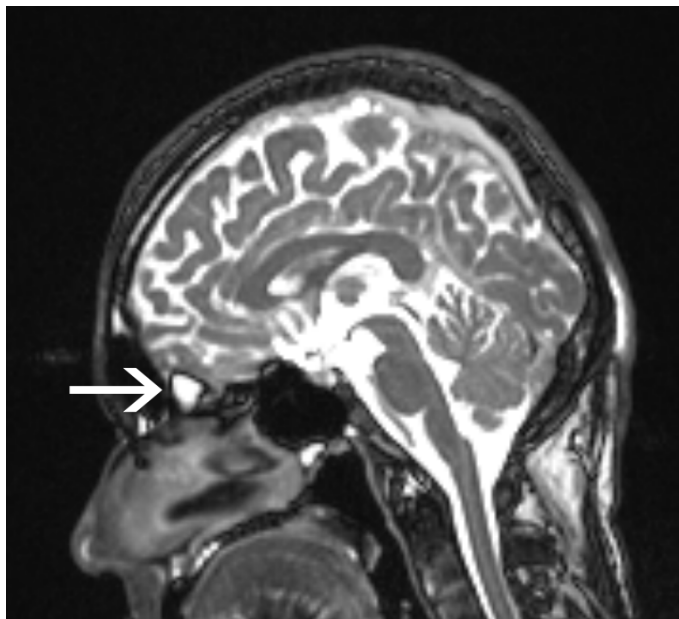


Figure 39: BSSFP image acquired with $\alpha = 30^\circ$, $TR = 2.99$ ms, and $T_{rf} = 270$ μs exhibiting banding artifact (arrow).

by multiple phase-cycled acquisitions [20]. Different phase-cycled images (e.g. $\Delta\phi = 0$, $\Delta\phi = \pi/2$, $\Delta\phi = \pi$ and $\Delta\phi = 3\pi/2$) are combined, yielding more homogeneous spectral profiles. There are different ways to combine the individual acquisitions and form the reconstructed image, e.g. maximum-intensity SSFP.

10 Summary

A new method of quantitative magnetization transfer imaging has been developed. Our in vivo measurements are based on bSSFP using a 1.5 T clinical MRI scanner. It has been found that the well-known bSSFP signal equation does not adequately describe the TR dependency of tissue signal. Magnetization transfer has to be taken into account. Using a two pool model for tissues a closed form solution describing the signal behavior including magnetization transfer was derived. The central assumption consisted in separating relaxation and exchange processes, allowing to use a matrix formalism. By numerical simulations of the exact equations it was shown that this approximation is justified. Thus, the solution could be used in a fitting procedure for a 3D data set acquired at 8 different flip angles and 8 different repetitions times.

Fitting measured data yields quantitative model properties that are comparable with published values. More precisely, these are the fractional size of the restricted pool F , the magnetization exchange rate k_f and the transverse relaxation time of the free pool $T_{2,f}$. These parameters and the calculated values for the longitudinal relaxation time of the free pool $T_{1,f}$ and the magnetization transfer ratio MTR remain stable over several measurements in one healthy volunteer.

For the first time, an MT imaging method produces several quantitative parameter maps not only for one brain slice, but for a whole 3D data set within a reasonable measurement period. The new method is considerably faster and a higher resolution compared to literature is used. In the future, the quantitative parameters may provide new information on the brain structure and pathological variations in brain matter. The method may as well provide more detailed information on cartilage [21].

I thank Oliver Bieri for all the discussions, suggestions and ideas that made this work possible.

11 Outlook

A reason for the discrepancies between our parameters and the literature values may be that in this study the relaxation rate $R_{1,r}$ was set equal to $R_{1,f}$. In further studies $R_{1,r}$ may be included in the fitting routine. Furthermore, our parameter estimates are very sensitive to the line shape $G(\Delta)$. In the future, the dependency of the estimates on $G(\Delta)$ may be analyzed and different values of $G(\Delta)$ could be chosen for white and gray matter regions, respectively.

Besides further investigations on the above described fitting routine, a generalization of the used principles is of interest. This comprises a possible use of the SSFP sequence.

11.1 SSFP signal with MT

In the general case with dephasing by the angle ϕ the gradient moments do not add up to zero after each sequence interval. The magnetization vector $\vec{M} = (M_{x,f} \ M_{y,f} \ M_{z,f} \ M_{z,r})$ is considered. A general rotation and dephasing matrix analogous to Eq. (6.4) and Eq. (3.7) has to be used. The matrix describing a spin flip by the angle α reads

$$R_x(\alpha) = \begin{pmatrix} 1 & 0 & 0 & 0 \\ 0 & \cos \alpha & \sin \alpha & 0 \\ 0 & -\sin \alpha & \cos \alpha & 0 \\ 0 & 0 & 0 & e^{-Wt} \end{pmatrix}, \quad (11.1)$$

the dephasing matrix is

$$R_z(\phi) = \begin{pmatrix} \cos \phi & \sin \phi & 0 & 0 \\ -\sin \phi & \cos \phi & 0 & 0 \\ 0 & 0 & 1 & 0 \\ 0 & 0 & 0 & 1 \end{pmatrix}, \quad (11.2)$$

and the relaxation matrix is given by

$$E(TR) = \begin{pmatrix} E_2 & 0 & 0 & 0 \\ 0 & E_2 & 0 & 0 \\ 0 & 0 & E_{1,f} & 0 \\ 0 & 0 & 0 & E_{1,r} \end{pmatrix}, \quad (11.3)$$

where $E_2 = e^{-TR/T_{2,f}}$, $E_{1,f} = e^{-R_{1,f}TR}$ and $E_{1,r} = e^{-R_{1,r}TR}$. The exchange matrix A is given by Eq. (6.2).

Assuming that relaxation and exchange can be separated, the eigenvalue equation becomes

$$\vec{M}^+(\infty) = R_x[I - R_z A E R_x]^{-1} A \vec{M}_0 \quad (11.4)$$

in case the relaxation takes place before the exchange, and

$$\vec{M}^+(\infty) = R_x[I - R_z E A R_x]^{-1} \vec{M}_0 \quad (11.5)$$

in case the exchange takes place before the relaxation, where

$$\vec{M}_0 = \begin{pmatrix} 0 \\ 0 \\ M_{0,f}(1 - E_{1,f}) \\ M_{0,r}(1 - E_{1,r}) \end{pmatrix} \quad (11.6)$$

The transversal components of the solution to Eq. (11.4) can be reduced to the same form as Eqs. (3.16) and (3.17):

$$M_x^+(\infty) = M_0 \sin \alpha \frac{G(1 - E_2 \cos \phi)}{C \cos \phi + D} \quad (11.7)$$

and

$$M_y^+(\infty) = M_0 \sin \alpha \frac{GE_2 \sin \phi}{C \cos \phi + D}, \quad (11.8)$$

where

$$G = (1 - E_{1,f})BM_{0,f} + (1 - E_{1,r})(1 - f_k)M_{0,r}, \quad (11.9a)$$

$$C = -E_2A + E_2E_{1,f}B - \cos \alpha E_2(A - E_{1,f}B), \quad (11.9b)$$

$$D = A - E_{1,f}E_2^2B + \cos \alpha(E_2^2A - E_{1,f}B). \quad (11.9c)$$

Furthermore,

$$A = 1 + F - Ff_wE_{1,r} + f_kf_wE_{1,r}, \quad (11.10a)$$

$$B = 1 + Ff_k - f_kf_wE_{1,r} + Ff_kf_wE_{1,r}, \quad (11.10b)$$

$$f_k = e^{-(k_f+k_r)TR} =: e^{-kTR}, \quad (11.10c)$$

$$f_w = e^{-WT_{rf}}, \quad (11.10d)$$

where $M_{0,f} = 1$, $M_{0,r} = FM_{0,f}$, $E_2 = e^{-t/T_{2,f}}$, $E_{1,f} = e^{-R_{1,f}TR}$ and $E_{1,r} = e^{-R_{1,r}TR}$. Integration thus yields the SSFP signal with MT

$$\langle M_T \rangle = M_0 \frac{G \sin \alpha}{C} \left(\frac{C + DE_2}{\sqrt{D^2 - C^2}} - E_2 \right), \quad (11.11)$$

analogous to Eq. (3.19).

11.2 SSFP signal behavior

The dependency of the SSFP signal on the flip angle and the repetition time are shown in Fig. 40. The simulated off-resonance signals can now be compared to calculations (Fig 41). The signal without saturation corresponds to the well-known SSFP signal (Eq. 3.15) and the signal with saturation shows good agreement with the calculated SSFP signal including MT (Eqs. 11.7 and 11.8).

The bSSFP signal is 40 % to 50 % stronger than the SSFP signal and the signal maximum occurs at a 5° to 10° higher flip angle as can be seen in Fig. 42 for white matter, $TR = 3.09$ ms and $T_{rf} = 400$ μ s.

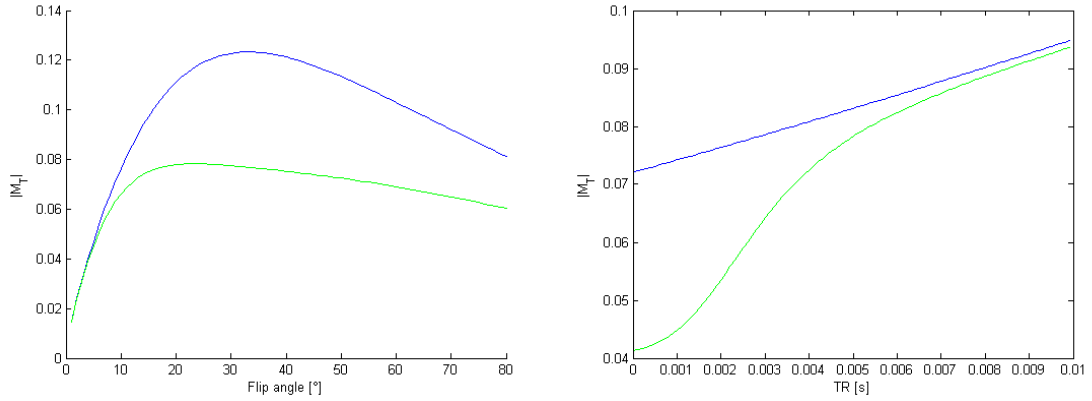


Figure 40: Simulated SSFP signal as a function of α (left) and TR (right). Blue curves: without saturation, green curves: with saturation.

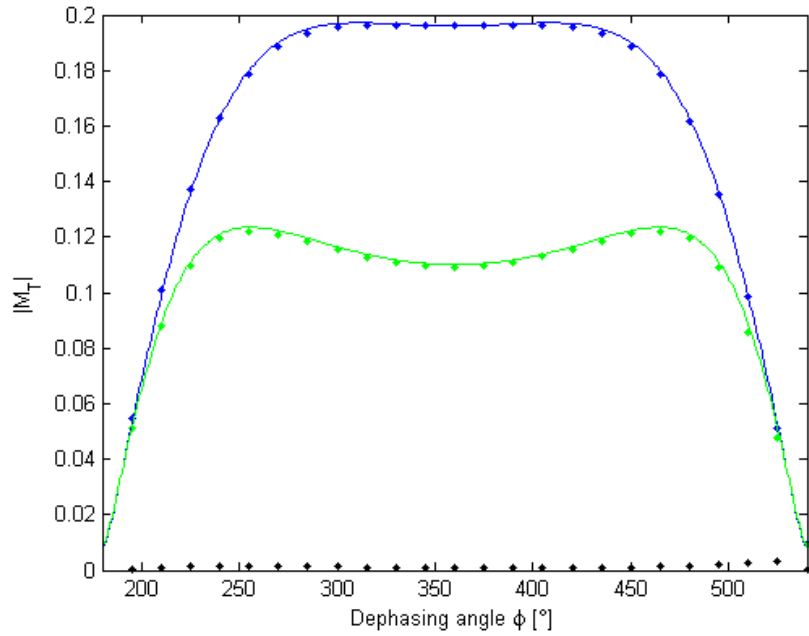


Figure 41: Off-resonance simulation and calculation for white matter, $TR = 3.5$ ms, $T_{rf} = 340$ μ s and $\alpha = 40^\circ$. Blue curve: SSFP signal without saturation, green curve: SSFP signal with saturation (dotted lines: simulated, solid lines: calculated) black dotted curve: difference of simulated values and calculated values with saturation.

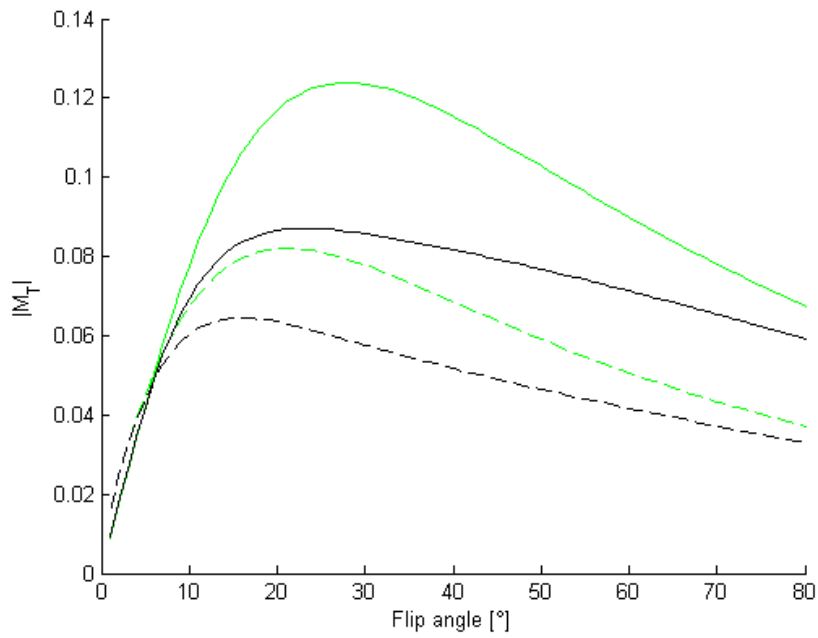


Figure 42: Green curves: signal without MT. Black curves: signal with MT. Both curves are calculated for bSSFP (solid lines) and SSFP (dashed lines). $TR = 3$ ms, $T_{rf} = 640$ μ s, $R_{1,f} = 1.71$ s^{-1} , $T_{2,f} = 81$ ms, $R_{1,r} = 1$ s^{-1} , $F = 0.157$ and $k_f = 4.45$ s^{-1} .

References

- [1] R. Freeman. *Magnetic resonance in chemistry and medicine*. Oxford 2003.
- [2] F. Bloch. Nuclear induction. *Phys. Rev.* 1946; 70: 460-474.
- [3] E. T. Jaynes. Matrix treatment of nuclear induction. *Phys. Rev.* 1955; 98: 1099-1105.
- [4] H. Y. Carr, E. M. Purcell. Effects of diffusion on free precession in nuclear magnetic resonance experiments. *Phys. Rev.* 1954, 94(3): 630-638.
- [5] S. Ljunggren. A simple graphical representation of Fourier-based imaging methods. *J. Magn. Reson.* 1983; 54: 338-343.
- [6] J. Pauly, D. Nishimura, A. Mackovski. Analysis of small tip angle excitation. *J. Magn. Res.* 1989; 81: 43-56.
- [7] K. Scheffler. A pictorial description of steady-states in rapid magnetic resonance imaging. *Concepts in Magn. Res.* 1999; 11(5); 291-304.
- [8] E. M. Haake et al. *Magnetic resonance imaging*. Wiley-Liss 1999.
- [9] Y. Zur, S. Stokar, P. Bendel. An analysis of fast imaging sequences with transverse magnetization refocussing. *Magn. Reson. Med.* 1988; 6: 175-193.
- [10] O. Bieri, K. Scheffler. On the origin of apparent low tissue signals in balanced SSFP. *Magn. Reson. Med.* 2006; 56: 1067-1074.
- [11] S. D. Wolff, R. S. Balaban. Magnetization transfer contrast (MTC) and tissue water proton relaxation in vivo. *Magn. Reson. Med.* 1989; 10: 135-144.
- [12] P. Tofts. *Quantitative MRI of the brain*. Wiley 2003.
- [13] R. M. Henkelman, X. Huang, Q. S. Xiang, G. J. Stanisz, S. D. Swanson M. J. Bronskill. Quantitative interpretation of magnetization transfer. *Magn. Reson. Med.* 1993; 29: 759-766.
- [14] R. Grossman, J. M. Gomori, K. N. Ramer, F. J. Lexa, M. D. Schnall. Magnetization transfer: theory and clinical applications in neuroradiology. *RadioGraphics* 1994; 14; 279-290.
- [15] S. J. Graham, R. M. Henkelman. Understanding pulsed magnetization transfer. *J. Magn. Reson. Imaging* 1997; 7: 475-482.
- [16] J. G. Li, S. J. Graham, R. M. Henkelman. A flexible magnetization transfer line shape derived from tissue experimental data. *Magn. Reson. Med.* 1997; 37: 866-871.
- [17] J. G. Sled, G. B. Pike. Quantitative interpretation of magnetization transfer in spoiled gradient echo MRI sequences. *J. Magn. Reson.* 2000; 145: 24-36.
- [18] J. G. Sled, G. B. Pike. Quantitative imaging of magnetization transfer exchange and relaxation properties in vivo using MRI. *Magn. Reson. Med.* 2001; 46: 923-931.

-
- [19] S. C. L. Deoni, T. M. Peters, B. K. Rutt. High-resolution T_1 and T_2 mapping of the brain in a clinically acceptable time with DESPOT1 and DESPOT2. *Magn. Reson. Med.* 2005; 53: 237-241.
- [20] N. K. Bangerter, B. A. Hargreaves, S. S. Vasanaawala, J. M. Pauly, G. E. Gold, D. G. Nishimura. Analysis of multiple-acquisition SSFP. *Magn. Reson. Med.* 2004; 51: 1038-1047.
- [21] D. K. Kim, T. L. Ceckler, V. C. Hascall, A. Calabro, R. S. Balaban. Analysis of water-macromolecule proton magnetization transfer in articular cartilage. *Magn. Reson. Med.* 1993; 29: 211-215.
- [22] J. Leupold. Neue Methoden zur frequenzselektiven Kernspintomographie mit TrueFISP-Sequenzen. Albert-Ludwigs-Universität, Freiburg im Breisgau, 2005.
- [23] U. A. Ludwig. Entwicklung und Optimierung leiser Magnetresonanz-Methoden für funktionelle Untersuchungen. Albert-Ludwigs-Universität, Freiburg im Breisgau, 2002.
- [24] M. T. Vlaardingerbroek, J. A. den Boer. *Magnetic resonance imaging*. Springer 2003.
- [25] R. M. Henkelman, G. J. Stanisz, S. J. Graham. Magnetization transfer in MRI: a review. *NMR Biomed.* 2001; 14: 57-64.
- [26] P. A. Rinck. *Magnetresonanz in der Medizin*. ABW Wissenschaftsverlag 2003.
- [27] J. Lissner, M. Seiderer. *Klinische Kernspintomographie*. Ferdinand Enke Verlag 1987.
- [28] D. G. Mitchell. *MRI principles*. Saunders 1999.
- [29] R. Freeman, H. Hill. Phase and intensity anomalies in Fourier transform NMR. *J. Magn. Reson.* 1971; 4: 366-383.